Chem Soc Rev

Chemical Society Reviews

www.rsc.org/chemsocrev

Volume 42 | Number 12 | 21 June 2013 | Pages 4845–5620

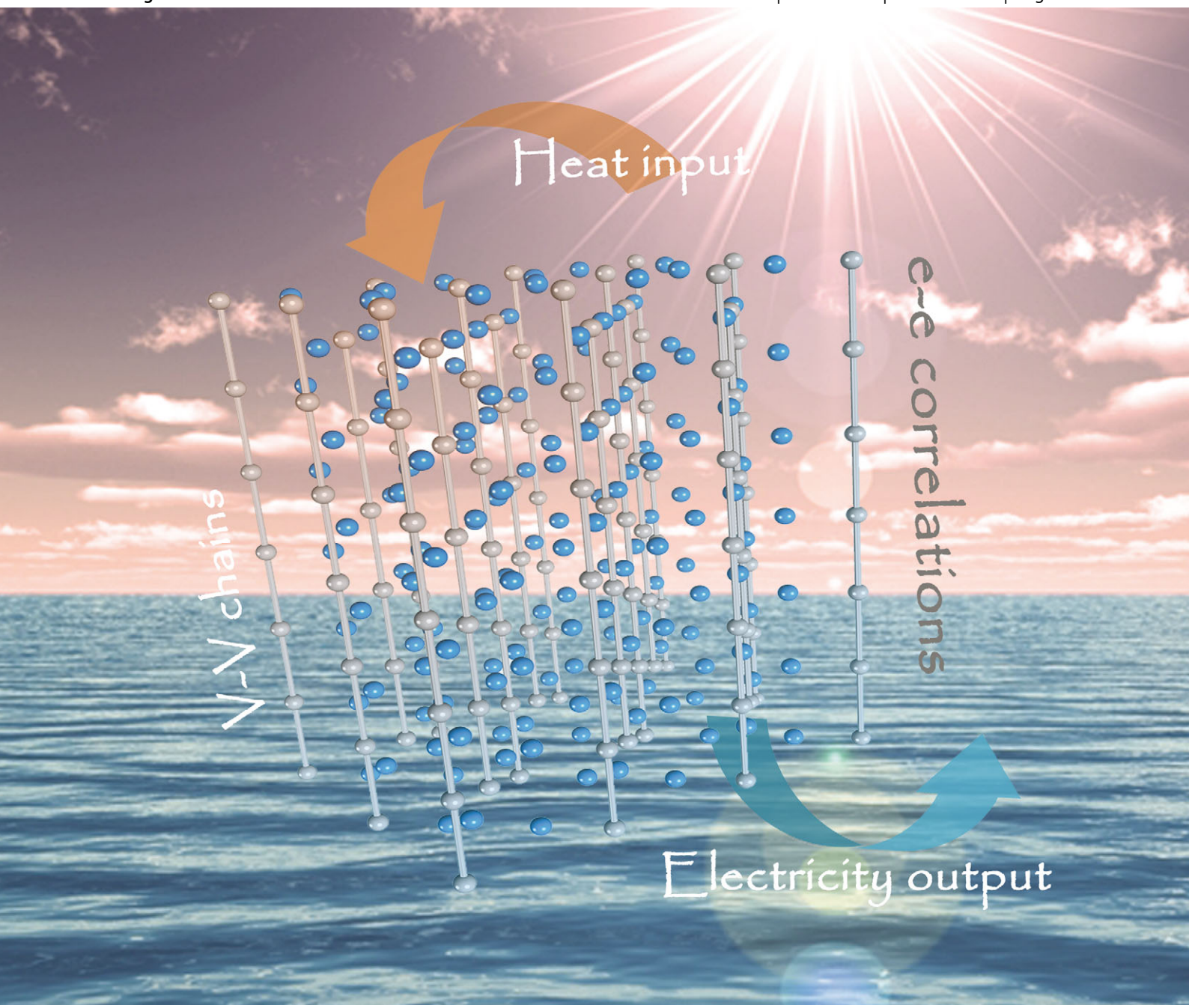

ISSN 0306-0012

RSC Publishing

REVIEW ARTICLE

Changzheng Wu, Feng Feng and Yi Xie

Design of vanadium oxide structures with controllable electrical properties for energy applications

Chem Soc Rev

RSC Publishing

REVIEW ARTICLE

View Article Online
View Journal | View Issue

Cite this: *Chem. Soc. Rev.*, 2013, **42**, 5157

Design of vanadium oxide structures with controllable electrical properties for energy applications

Changzheng Wu, Feng Feng and Yi Xie*

The electrical properties of inorganic materials has been a long-standing pursued research topic, and successfully controlling the electrical property of an inorganic material has attracted significant attention for a wide range of energy-related applications, covering energy storage, energy conversion and energy utilization. During the few past decades, vanadium oxides have been studied to gain a clear picture of how microstructural characteristics generating the e–e correlations influence the electronic structure of a material, through which the charge concentration, electrical conductivity as well as the metal–insulator transition (MIT), *etc.*, can be precisely controlled, giving promising signs for constructing energy-related devices. In this review, we present an extensive review of the engineering of the microstructures of vanadium oxides with control of their electrical properties, and with attempts to rationally construct energy-related devices, such as aqueous lithium ion batteries, supercapacitors for energy storage, and thermoelectric generators for energy conversion. Furthermore, the MIT performance of vanadium oxides has also seen tremendous advantages for the applications of ''smart windows'' and magnetocaloric refrigerators for energy utilization. Collectively, progresses to date suggest that in vanadium oxide systems, the electrical properties, including electrical conductivity, carrier concentrations, and the MIT performance, were all strongly dependent on the microstructural characteristics at the atomic scale, which have presented extensive promising energy applications covering energy storage, energy conversion and energy utilization.

Received 11th December 2012

DOI: 10.1039/c3cs35508j

www.rsc.org/csr

1. Introduction

The electrical properties of materials are long-standing important issues in fundamental solid-chemistry fields.

Hefei National Laboratory for Physical Sciences at Microscale, University of Science and Technology of China, Hefei, Anhui 230026, P. R. China.
E-mail: yxie@ustc.edu.cn

Changzheng Wu

Changzheng Wu obtained his BS degree (2002) and PhD degree (2007) in the Department of Chemistry at University of Science and Technology of China. He has since worked as a post-doctoral fellow in the Hefei National Laboratory for Physical Sciences at Microscale. From 2009, Dr Wu joined the Department of Chemistry, University of Science and Technology of China as an associate professor. His current interests include solution-phase assembly, metal–insulator transition (MIT) materials and their theoretical understanding.

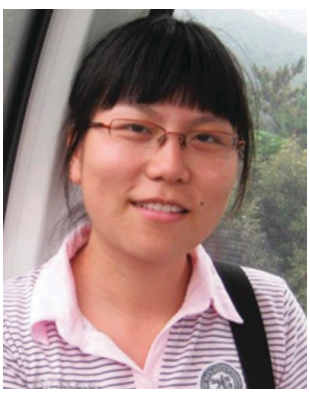

Feng Feng

Feng Feng received her BS degree in Applied Chemistry from Jiangnan University, China, in 2010. She is currently pursuing her PhD in inorganic chemistry at the University of Science and Technology of China, under the supervision of Prof. Yi Xie and Prof. Changzheng Wu. Her current interests include the synthesis and characterization of nanostructures, especially vanadium oxides, and their energy-related application for energy storage and conversion.

Moreover, electrical properties, such as the electrical conductivity, carrier concentrations and electrical switching, have a great influence on employing the functional materials in many fascinating applications, including electrochemical applications, energy storage processes, thermoelectric devices and smart windows based on metal–insulator transition (MIT) and so forth.[1–4] The intrinsic electrical property is strongly related to the electronic structure that arises from the electronic interactions in the given crystal lattices forming the different energy bands in the solids.[5,6] Monitoring of the spin, charge, lattice and orbital degrees of freedom allows an alternative way to control the electrical properties.[7,8] A specific and very important role is played by the design of crystal structures, through which rich electrical parameters of the material can be modulated accordingly.[9] In this regard, structural lattice perturbation would simultaneously activate the spin, charge, and/or orbital of a material, and thus it would provide an effective way to modulate its band gap width, creating phase transformations among metallic, semiconducting, and insulating states.[10] In this case, the subtle variation of atomic positions in electron–electron correlated systems would usually result in a dramatic change of the electrical property.[11,12]

Vanadium oxides are an ideal material platform for investigating how the electronic structure influences the electronic structure of a material undergoing slight structural change. For example, monoclinic/rutile vanadium dioxides VO_2(M/R) are well-known prototype materials and have been used for interpreting correlation effects in solids since their discovery in the 1950s.[13,14] VO_2(M) undergoes a fully reversible MIT between VO_2(M) and VO_2(R), with a huge temperature-induced change in resistivity, in which the small distortion of the infinitely linear V–V chains in VO_2(R) to the zigzag chains in VO_2(M) accounts for the occurrence of the MIT.[15,16] In effect, the outer 3d electrons, being either localized or itinerant, in vanadium oxides are dependent on the electron–electron correlation strengths of the cation–cation interactions. As Goodenough has demonstrated, the critical separation value ($R_c \approx 2.93 \pm 0.04$ Å) of the 3d electron coupling interaction for both neighboring V^{3+}–V^{3+} and V^{4+}–V^{4+} ions can be deduced from semiempirical expressions and the properties of several isostructural series of compounds, which have been well confirmed for an integral number of 3d electrons per cation in vanadium oxides.[17] In this case, when the separation value R is larger than R_c, the electrons are localized, while the 3d electrons are itinerant when $R < R_c$. Since then, the critical V–V interaction value has played a crucial role in understanding how the atomic lattices influence the correlation effects in vanadium oxides, and also has paved a way to modulate the electron–electron correlations. For example, in VO_2(R), the infinite chains with a V–V distance of 0.288 nm ($<R_c$) along the rutile c-axis (c_R-axis) makes the d-orbital electrons become shared by all of the metal V atoms along this direction, leading to the metallic behavior. While in the VO_2(M) structure, the vanadium atoms form dimers with two values of 0.262 nm ($<R_c$) and 0.316 nm ($>R_c$) to result in the insulator/semiconductor behavior of VO_2(M).[18] Designing the structural parameters of atomic lattices could effectively modulate their electrical properties.

The tunable electrical properties have been one of the main barriers to further improvements in energy-related fields and are expected to remain so for the foreseeable future. As is known, the dominant energy-related applications, such as energy storage including both lithium ion batteries and supercapacitors, and energy conversion in the form of thermoelectric devices, are all significantly dependent on the intrinsic electrical properties.[19,20] During the electrochemical processes, the highly conducting electrode materials would receive a quick electrical response during the electrochemical processes, and also it would help to improve the utilization ratio of the active materials due to the presence of the conducting networks in the electrode.[21] The conducting behavior of the active material would facilitate electrochemical intercalation/deintercalation of Li^+ ions in a lithium ion battery, or improve the electron/charge diffusion coefficient in supercapacitors.[22,23] Furthermore, as an intriguing energy conversion technology, thermoelectric effects would directly convert the thermal energy to electrical energy;[24] and a superior thermoelectric performance depends on simultaneously achieving high electrical conductivity (σ), high thermoelectric power (S), and low thermal conductivity (κ).[25] All three parameters are dependent on the details of the electronic structure as well as the charge carrier-related properties with high performance. That is, the intrinsic electrical properties are indeed responsible for thermoelectric devices. In this regard, vanadium oxides provide an ideal material platform for tuning the intrinsic electrical properties due to the presence of rich electron–electron correlation effects, entailing their fascinating energy-related applications of energy storage, energy conversion and energy utilization.

With the above-mentioned concepts in mind, in this review, the fundamental materials chemistry, condensed matter physics and device developments enabling vanadium oxides to be promising candidates in energy-related applications are discussed.

Yi Xie

Yi Xie received her BS from Xiamen University (1988) and PhD from the University of Science and Technology of China (1996). She is now a Principal Investigator (PI) of Hefei National Laboratory for Physical Sciences at Microscale and a full professor of the Department of Chemistry, University of Science and Technology of China. She was appointed as the Cheung Kong Scholar Professor of inorganic chemistry in 2000, also a recipient of the China Young Scientist Award (2002) and China Young Female Scientist Award (2006). Her research interests are cutting-edge research at four major frontiers: nanotechnology, solid state chemistry, energy science and theoretical physics.

Initially, we describe the electronic nature of the MIT in vanadium oxides for understanding how the microstructural atomic lattices influence the electrical properties of vanadium oxides. We also survey the synthetic methodologies used to achieve a rich variety of vanadium oxide/hydroxide polymorphs. With the newly developed chemical methodologies, we unravelled a series of new-phased vanadium oxides and new synthetic mineral phases, providing a material platform for understanding the origin of electrical properties in vanadium oxides. In effect, precisely controlling the structural lattices in vanadium oxides would effectively influence the electrical properties, such as carrier concentrations and electrical conductivity, which opens new avenues for various energy storage and energy conversion applications, such as lithium-ion batteries, supercapacitors, and thermoelectrical applications. Moreover, controlling the microstructural lattices of vanadium oxides also influences the e–e correlations in the vanadium oxide system that would regulate the phase-transition performance of the vanadium oxides with a MIT behavior, which has shown tremendous advantages for the construction of "smart windows" and magnetic refrigeration for energy utilization applications.

2. Understanding electronic correlations in vanadium oxides

A series of vanadium oxides with strong electron–electron correlations exhibit MITs. Since Morin's first discovery of VO_2(M) in the 1950s,[26] vanadium oxides have received extensive interest for physically understanding the action role of electron–electron correlations in phase transition behavior, but also for a wide range of technological applications, such as Mott transistors, smart windows and energy devices, *etc.*[27] Up to now, well-known examples of non-stoichiometric vanadium oxides exhibiting the phase transition behavior belong to two categories: the general formula of V_nO_{2n+1} existing between V_2O_5 and VO_2, and the general formula of V_nO_{2n-1} for Magnéli-type vanadium oxide (named after Arne Magnéli[28]). The V_nO_{2n+1} family has less members compared to that of Magnéli phases, and typical members in the V_nO_{2n+1} family include V_6O_{13}, with an antiferromagnetic Neel temperature at 155 K and an abrupt change in electrical conductivity of the order of ten,[29] and V_3O_7, with phase transition temperature of 5.2 K.[30] Magnéli-type vanadium oxides are a homologous series of shear structures based on the VO_2(R) structure. Examples of Magnéli phases forming V_nO_{2n-1} ($3 \leq n \leq 10$) are shown in Fig. 1, including V_4O_7 (250 K), V_5O_9 (135 K), V_6O_{11} (170 K), V_7O_{13} (metallic) and V_8O_{15} (70 K) with different phase transition temperatures, respectively.[31,32] They undergo an abrupt structural transition from metallic to insulating states and *vice versa*, even keeping the global stoichiometry unchanged, forming rich family members of phase transition materials in vanadium oxides.

VO_2(M), belonging to V_nO_{2n-1} when $n = \infty$, is long-standing textbook example of systems that exhibit well-defined electrical switching properties in the form of a MIT, in which the electrical conductivity can change by up to five orders of magnitude.[33]

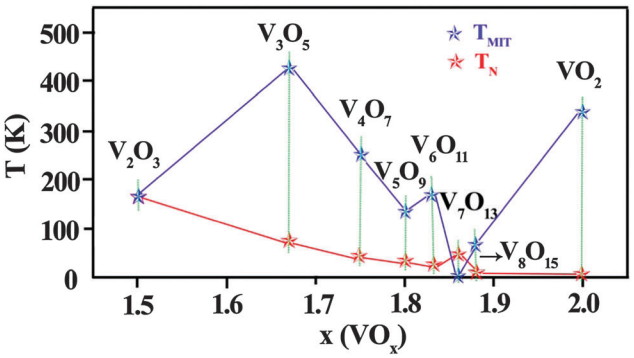

Fig. 1 MIT temperatures and the magnetic ordering temperatures in the Magneli phases. All the vanadium oxide members exhibit MITs, except V_7O_{13}.

Also, VO_2(M) is a prototype material for interpreting the electron–electron correlations,[34] in which the structural evolution picture upon the phase transition from VO_2(M) to VO_2(R) has been well understood. As is shown in Fig. 2a–b, for VO_2(M), there are two different V–V distances, 0.262 nm and 0.316 nm, which are the distances between the nearest vanadium atoms from the V–V dimers and the zigzag-type V atom chains along the c_R-axis, respectively. In this case, the larger V–V distance (0.316 nm) is much greater than the critical V–V interaction distance of 0.294 nm, resulting in the localization of d-orbital electrons inside the dimer, which gives to the insulating behavior of VO_2(M),[35] with a resistance of the order of 0.1 Ω m.[36] For tetragonal VO_2(R), all the vanadium ions are aligned into one line with an average nearest V–V distance of 0.288 nm, which is smaller than the 0.294 nm. Thus, the presence of infinite chains along the rutile *c*-axis (c_R-axis) with the nearest neighboring V–V distance of 0.288 nm leads to the d-orbital electrons being shared by all of the metal V atoms, giving the metallic behavior of VO_2(R)[37] with a low resistivity of about 10^{-6} Ω m.[38]

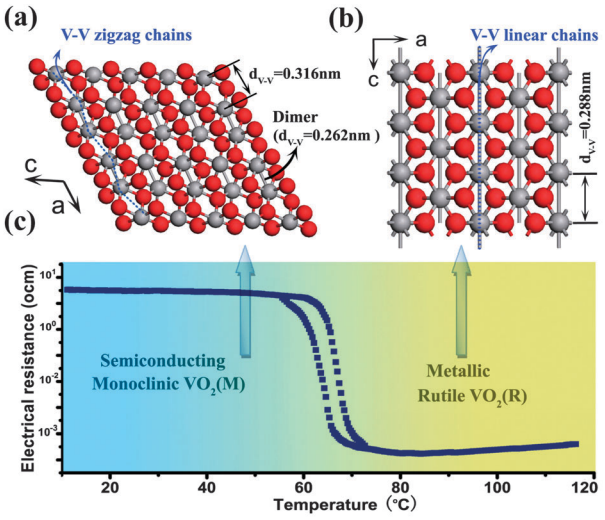

Fig. 2 Atomic crystal structure of VO_2(M): (a) projected along the *b*-axis of the monoclinic cell with the zigzag-type vanadium atom chains; (b) projected along *b*-axis of the rutile cell with the infinite linear V–V chains. (c) Temperature dependence of the resistivity based on the fully-reversible phase transition.

For the phase transition from VO_2(M) to VO_2(R), the slight distortion of the V–V linear chains to the zigzag pattern leads to the MIT process. Of note, the MIT process accompanies the benefits of huge temperature-induced changes in resistivity (Fig. 2c) and selective IR optical switching, in which low-temperature VO_2(M) is an insulator and allows infrared to transmit, while the high-temperature phase VO_2(R) is metallic and IR-blocking in the infrared region.[39] The fully reversible phase transition in VO_2(M)–VO_2(R) has thus attracted great interest in scientific and technological communities for the construction of smart devices, such as temperature sensors and energy efficient ''smart windows'', and also provides an ideal platform to understand the correlated effects in solids.[40] More importantly, the driving force of the phase transition has been a long-standing dispute, whether just the electronic correlation is strong enough to localize the electrons forming a Mott–Hubbard insulator (Mott model), or the structural distortions alone can induce the insulating phase (Peierls model).[41] The former is based on strong e–e correlation effects; the latter anticipates a lattice instability triggered by electron–phonon interactions within a reduced-dimensional system.[42,43] To clarify the exact physical picture lying behind the MIT process, both theoretical and *in situ* experimental efforts have been made in recent years to understand the nature of the insulator–metal transitions.[44]

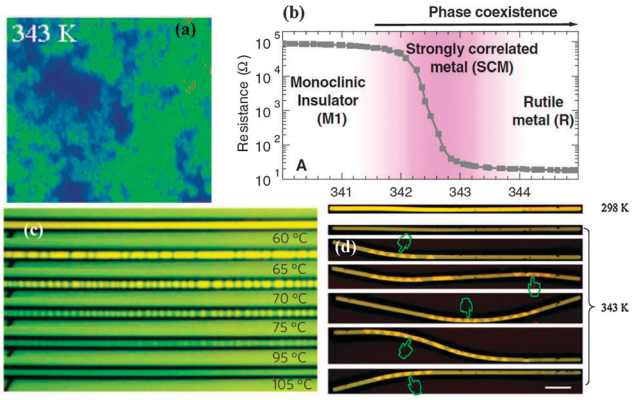

Fig. 3 (a) The image obtained by a scattering scanning near-field infrared microscope, which shows the coexistence of metallic (green) and insulating (dark blue) phases in the VO_2 thin film. (b) The resistance–temperature curve shows the phase transition, where the shaded area highlights the existence of the strongly correlated metal (SCM) with a divergent quasi-particle mass and an optical pseudogap. (Adapted with permission from ref. 45, Copyright 2007 American Association for the Advancement of Science (AAAS).) (c) Optical microscopy image shows the phase domain evolution of the different temperatures upon the MIT in VO_2 nanobeams, clearly showing metallic domains (darker) appearing, widening and merging during warming. (d) Strain engineering domains in a flexible VO_2 microbeam. (Adapted with permission from ref. 16, Copyright 2009 Nature).

2.1 Direct imaging of the insulator-to-metal transition during the structural phase transition process

Great efforts have been made during the past few decades to directly observe the metallic state and insulating state during the insulator-to-metal transition, where it has been possible to observe the local microscopic atomic-scale lattices using a high-resolution transmission electron microscope (TEM). The structural resemblance between the metallic and insulating phases increases the difficulty for directly imaging the MIT process. For example, monoclinic and rutile VO_2 have different crystal systems, but their crystal lattices are of great similarity. The only difference between these two structures is the displacement of the vanadium atoms from the infinite lines in the rutile form compared to the monoclinic phase. As long as the direct recognition of these two kinds of phase domains and the domain evolution upon phase transition remain a challenge, it certainly helps to understand the nucleation process, structural change evolution as well as the influence of the electron–electron correlations during the phase transition. *In situ* far-field infrared spectroscopy (FFIS) (Fig. 3a) provides an efficient way to directly distinguish the two kinds of monoclinic and rutile phase domains as well as to understand the electron correlated behavior in prototypical correlated insulators of vanadium dioxide.[45] In the VO_2 thin film, the temperature-dependent resistivity curve shows the electrical change in the vicinity of the phase transition point corresponding to the multiple phase coexistence. Also, the FFIS image clearly shows the gradual appearance of the metallic regions (light blue, green, and red) due to the higher scattering near-field amplitude in the MIT regime of VO_2. In this work, the metallic puddles surrounded by the insulating phases were referred to as a ''strong correlated metal'', with the divergent quasi-particle mass with a pseudogap (Fig. 3b). The observed pseudogap in the ''strong correlated metal'' of VO_2 would lead to the collapse of electronically and/or magnetically ordered states, as well as the loss of long-range charge order,[46,47] thereby causing an abrupt resistivity change across the phase transition.

Therefore, work on samples with smaller sizes than the characteristic domain zone in the homogeneous limit helps to reveal intrinsic physical properties that are hidden in multiple-domain samples.[48] In this regard, freestanding nanowires exhibit rather distinct electrical and optical properties. As shown in Fig. 3c, devices made from freestanding nanowires will display an abrupt change of optical reflection, with darker reflection referring to a metallic phase and brighter reflection to an insulating phase.[49] Thus, the optical change has been a powerful tool for tracking the local microscopic structure information in monoclinic and rutile VO_2. Optical imaging of the single-domain nanobeam entails the benefits for investigation of the physical properties with response to strain at smaller length scales, which has received intense research attention.

With the benefits of optical imaging of the metallic and insulating phases, the electronic-structural coupled phase transition of VO_2 could be clearly revealed, offering an interesting platform to study its phase transition with response to the strain effect. For vanadium dioxides, upon passing through the phase transition, the vanadium atoms will shift from the infinite lines in the rutile structure, forming the tilted dimer with respect to the c_R-axis, causing the structural expansion (by 1%) along this direction.[50] Due to the presence of abrupt changes of the lattice constant, before/after the phase transition, the uniaxial compressive (tensile) stress along the

rutile *c*-direction would facilitate the phase transformation into metallic rutile (insulating monoclinic) VO_2 phase.[51] In this regard, the phase transition behavior between the freestanding and clamped nanobeam exhibits a significantly different electrical behavior. Electrical measurement on the unstrained sample would display a sharp drop of resistance in the vicinity of the MIT temperature for the single-domain nanobeam. However, for the clamped VO_2 nanobeams with the multiple-domain device, the temperature-dependent resistivity would cover a wide phase transition temperature range due to the effect of the strain on the nanobeams. The optical microscopy captured the phase transition process with a broadening transition temperature; and the broadened MIT temperature range is due to the presence of multiple domains in the clamped VO_2 nanobeam, originating from the strain/compression effect. Moreover, the strain effect could even lower the phase transition temperature to room temperature, paving the way for intriguing applications. Since the electronic states in the strongly correlated VO_2 is very sensitive to local strains under external stress, it also provides a new way to manipulate and engineer the functional domains. As shown in Fig. 3d, by simply modulating the local strain in a VO_2 nanobeam, metallic-insulating triangular domains can be precisely controlled for their appearance and elimination. As the metallic and insulating phases have distinctly different properties, strain-engineered VO_2 not only achieves collective and externally intriguing applications,[52] but also provides a fundamental understanding of the effect of electronic-structure correlations upon triggering the structural phase transition in VO_2.

2.2 *In situ* structural analysis of the structural phase transition process

The MIT occurs within a very short time scale, and recently time-resolved techniques are emerging as a tool to study the MIT.[53,54] In this regard, time is another vital parameter in advancing our understanding of sophisticated physical processes.[55] Available four-dimensional (4D) ultrafast electron microscopy has shown the ability to obtain sequences of snapshots with atomic-scale spatial resolution within 100 fs, and then four-dimensional (4D) femtosecond electron diffraction was introduced to investigate the dynamic behavior of the structural transition from the initial monoclinic to the final tetragonal phase in crystalline VO_2. The ultrafast TEM technique (Fig. 4) directly reveals a dynamic molecular picture. The structural transition from VO_2(M) to VO_2(R) firstly involves dilation of the primary vanadium–vanadium bond with local displacements in the fs and ps time scale, followed by long-range shear rearrangements in a longer time scale of the sub-ns time scale and at the speed of sound. That is to say, the femtosecond electron diffraction clearly shows that the V–V bond dilation and local V atom displacement is the initial step of the insulator-to-metal transformation, mapping out a dynamic molecular picture by directly monitoring the coordinates of atoms in the insulator-to-metal transformation process.[56,57] This scenario of structural evolution clearly describes the

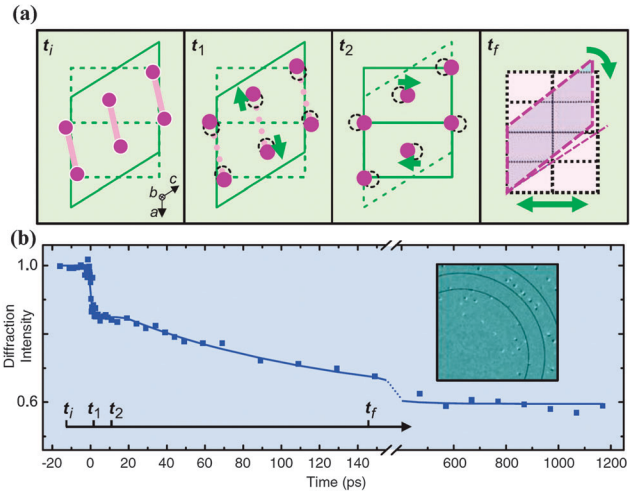

Fig. 4 Four-dimensional (4D) femtosecond electron diffraction revealed the transitional structures during the ultrafast phase transformation of VO_2. (a) Shown are frames at the corresponding times (t_i, t_1, t_2, and t_f) of structural changes, showing the structural change steps with a sequence of first involving local displacements in the fs and ps time scale, and the following long-range shear rearrangements in the sub-ns time scale. (b) The time-dependent diffraction intensity curve reflects the stepwise atomic motion within the unit cell in smaller length scales, and the shear motion in larger length scales. Inset is the difference in static X-ray patterns between the monoclinic and rutile VO_2, showing the macroscopic shear (angular) displacement. (Adapted with permission from ref. 56, Copyright 2007 AAAS).

Peierls model, in that the structural distortions induce the initial driving force of the MIT process.

Along this line, we also performed synchrotron X-ray absorption fine structure spectroscopy (XAFS) for *in situ* observation of the structural transformation process. XAFS has been widely regarded as a powerful tool for investigating the local structural characteristics of condensed matters, providing direct insight into the phase transition mechanism of VO_2(M). We developed an *in situ* temperature-dependent XAFS technique to measure the vanadium K-edge in order to monitor the structural phase transition of VO_2(M) in real time.[58] Obvious spectroscopic evolution could be observed in Fig. 5a, revealing the spatial changes of atomic lattice structures throughout the phase transition process. In fact, upon the phase transition process from VO_2(M) to VO_2(R), the V–V pairs in the chains not only undergo the dimerization of V–V pairs and tilting from the *c*-axis, but also twist from the zigzag-type to linear chains. This phenomenon provides an important parameter, *i.e.*, the δ angle of the nearest V–V coordination (Fig. 5b), to quantitatively describe the two-dimensional structural spatial changes. The dimerization of the V–V pairs, with a δ angle, has a close correlation with the measurement results of electrical resistance. The *in situ* XAFS results suggested that the local structural rearrangement around the V atoms provides a key factor to narrow the insulating band–gap, suggesting a structurally-driven VO_2 MIT process. Also, first-principle calculations revealed that the atomic structural changes directly induce the formation of the metallic phase of VO_2(R) from the semiconducting VO_2(M), further confirming that the MIT process

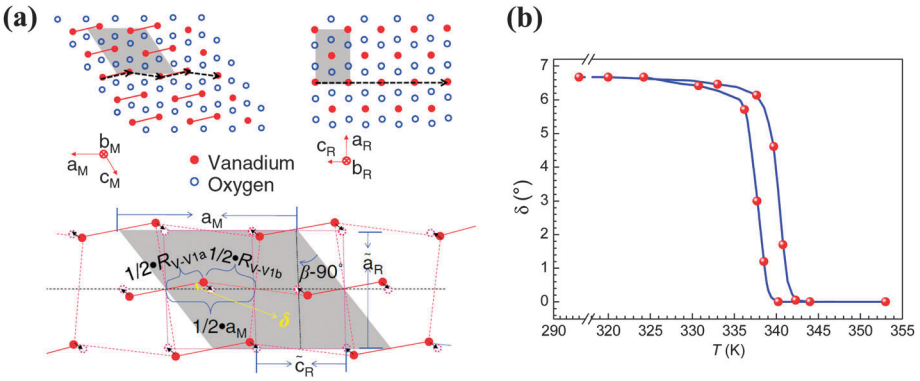

Fig. 5 *In situ* XAFS investigation into the MIT process in VO_2(M). (a) The top panel shows the microscopic atomic structures of VO_2(M) and VO_2(R) projected along [010]. The distortion of vanadium atoms is outlined by black arrows along the a_M axis (c_R). The bottom panel shows the motions of the V atoms and the relations of the unit cell parameters between the two phases. The twisted angle of the V–V pairs is noted as δ. (b) Twisted angle δ *versus* the temperature in a thermal circulation of heating and cooling, where the *in situ* XAFS gives a clear physical scenario for the structural change process on passing through the MIT. (Adapted with permission from ref. 58, Copyright 2010 American Physics Society).

originates from the structural changes. These results are also significant for connecting lattice structures and electronic properties in the electron–electron correlation phenomena.

In situ XAFS also provides direct insight into the local structural evolution of W-doped VO_2, which has been a well-known material model with a lower MIT temperature.[59] The unveiled isolated W dopant possesses an intrinsically symmetric tetragonal-like structure (Fig. 6a), which drives the de-twisting of the nearby asymmetric VO_2(M) lattice towards the rutile structure. These W-encompassed VO_2(R) regions act as growth nuclei for the "metallic puddles" (Fig. 6b), and these nuclei propagated through the host matrix to lower the thermal activation energy across the phase transition.

In this section, both the direct imaging and *in situ* structural analysis are powerful tools for describing the MIT process. The direct imaging technology, such as the *in situ* far-field infrared spectroscopy (FFIS) and optical microscopy, clearly depicts the metallic and insulating states in the phase coexistence conditions, enabling us to directly view the phase domain evolution upon the phase transition. Obviously, it allows us to understand the electron–electron and the electron–phonon correlations in the MIT process. With respect to the *in situ* structural analysis of the structural phase transition, including the ultrafast ED, *in situ* XAFS, *etc.*, it provides us with the possibility of understanding the local microstructure evolution during the MIT process, providing vital structural information, such as the role of structural characteristics in determining the phase transition behavior. Even so, the interplay of the microscopic degrees of freedom, such as spin, charge, orbit, and lattice, contributing to the phase transition of vanadium dioxides, still requires deep investigation. Working out the exact details of the driving force of the phase transition behavior still poses a true challenge to modern chemical and physical scientists.

3. Synthesis of VO_2(M) as the prototype metal–insulator transition material

As the prototype material for correlated systems, synthetic methodologies for the preparation of high-quality VO_2(M) have been a long-term pursuit. In fact, the phase transition behavior is highly dependent on the sample quality of VO_2(M),[60] which adds the importance of the development of new available synthetic methodologies. However, the library of synthetic

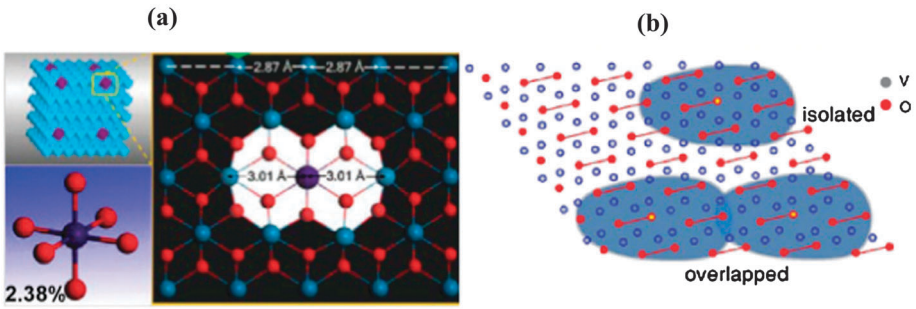

Fig. 6 *In situ* XAFS investigation of the MIT process in W-doped VO_2(M). (a) Structural models of the representative doped concentrations. The white area displays the local structural evolution around the W atoms. The W–W distances and [WO_6] octahedral geometries are shown in the left pane, respectively. (b) The schematic diagram of concentration scaled influences of W-doped VO_2, from which the low concentration with isolated dopants and the high concentration with interactional dopants can be clearly revealed by the *in situ* XAFS results and first-principle calculations. (Adapted with permission from ref. 59, Copyright 2012 Nature).

methodologies towards VO_2(M) seems to be very limited, of which solid-state reactions are the most usual synthetic route to VO_2(M).[61,62] For the detailed synthetic process, the formation of VO_2(M) has particular specificity. Intrinsically, it can be known that VO_2(M) and VO_2(R) are the same materials with two different thermodynamic states at different environmental temperatures. VO_2(M) could only be formed by the phase transition from the high-temperature VO_2(R) phase due to the fully-reversible phase transition process as well as an adopted synthesis temperature of higher than 68 °C. Controlling the formation of VO_2(R) represents an exclusive way to form VO_2(M) when the product is cooled to room temperature. In this regard, to achieve new available synthetic methodologies of VO_2(M), VO_2(R) should be taken as the foremost consideration. Since the synthetic temperatures of the reaction processes are usually much higher than the phase transition temperature (68 °C), only VO_2(R) can exist in such high reaction-temperature conditions.

The rutile structure, with 1 × 1 tunnel octahedra, is well known as the thermodynamically stable phase among structures of transition-metal dioxides (MO_2, M = Ti, Mn, V, *etc.*).[63,64] There is no exception for VO_2(R) as the thermodynamically stable phase, as can be evidenced by the calculation results. The hybrid density functional theory revealed that the VO_2(R) has a formation energy value of −6.93 eV per VO_2 unit, which is lower than that of other type of VO_2, such as VO_2(B), paramontroseite VO_2, *etc.* (Fig. 7a),[65] revealing the thermodynamically stable phase of VO_2(R). For obtaining the most thermodynamically stable phase, a high reaction temperature is usually the prerequisite condition. For example, rutile TiO_2 is the most stable phase compared to metastable anatase and brookite TiO_2, and in effect anatase and brookite TiO_2 would eventually convert to rutile TiO_2 through the high temperature treatment.[66] Along this line, heating the vanadium-including precursors at a relatively higher temperature usually leads to the formation of VO_2(R). For example, when using the traditional solid-state reaction routes, such as the sol–gel route,[67] direct annealing vanadium-including precursors,[68] and vapor transport method,[69] *etc.*, all lead to the formation of VO_2(M). Moreover, VO_2(R) has V^{4+} with a valence state of +4, which is one of the middle valence states of elemental vanadium, which covers the valence states of +2, +3, +4, and +5. In this case, how to control the valence states of the vanadium oxides poses a true challenge due to the high sensitivity of V^{4+} to be oxidized to V^{5+} or reduced to V^{3+}. To control the synthesis of VO_2(M), an inert gas atmosphere with a precisely controlled flow rate must be used, which adds the practical difficulty of achieving high quality VO_2(M) in a conventional laboratory. In a word, obtaining VO_2(M) as the product of a solid-state reaction requires the rigid synergic effects of an appropriate reaction temperature, an inert gas atmosphere, and a strict reaction time, which are not easy to control well, and so, new alternative methodologies are much needed.

3.1 New solid-state reaction pathway to VO_2(M)

As is known, a high reaction temperature is usually regarded as a prerequisite for obtaining the thermodynamically stable phase of a material.[70–72] As for the formation of VO_2(R), to control the valence states of vanadium oxides so that it is in the right valence state (+4) becomes a practical challenge. So, the relatively higher reaction temperature and maintaining the +4 valence state of the vanadium ions are two prerequisite conditions for achieving the thermodynamically stable phase among the vanadium dioxides.

3.1.1 Space confinement combustion route towards the target synthesis of VO_2(M). In consideration of the above analysis, we developed a new strategy to achieve VO_2(M). We found that the combustion of ethanol solution provides an ideal reaction environment for the formation of VO_2(M).[73] A combustion process has sufficient thermal energy with a relatively high temperature, which would favorably overcome

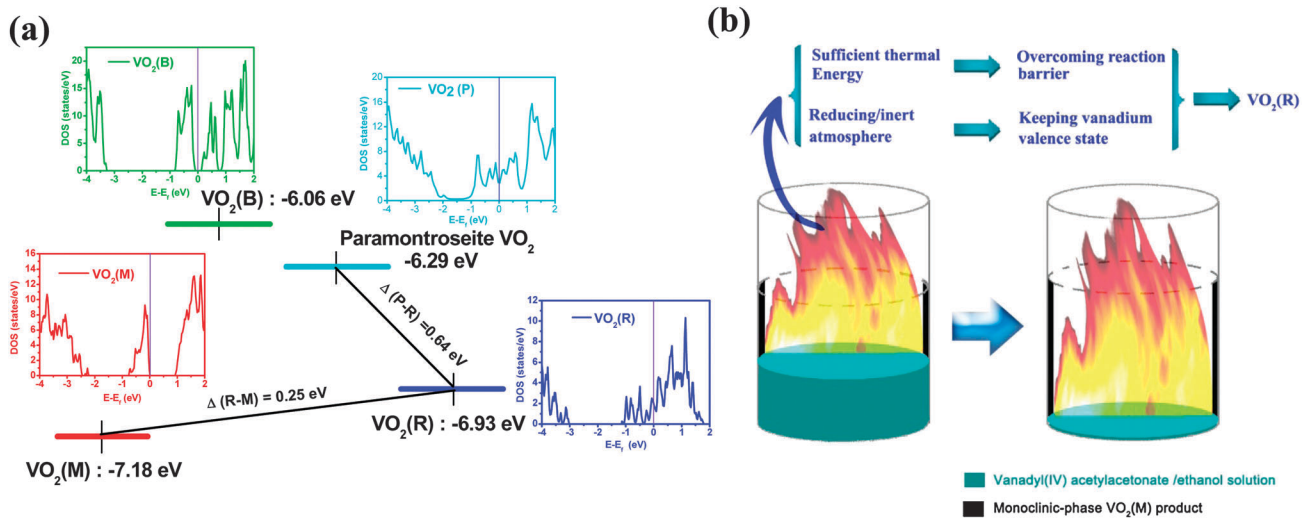

Fig. 7 Space-confinement combustion route towards VO_2(M). (a) The calculated formation energy for paramontroseite VO_2, VO_2(M), VO_2(R) and VO_2(B) according to the hybrid density functional theory, from which one can see that the VO_2(M) and VO_2(R) have the relatively lower formation energies among the VO_2 family. (b) Schematic illustration of confined-space combustion towards VO_2(M). (Adapted with permission from ref. 73, Copyright 2010 Wiley-VCH Verlag GmbH & Co.)[73]

the energy barrier to form the thermodynamically stable phase. Meanwhile, the confined-space combustion of ethanol produces a mild reductive species that can control the valence state of vanadium in the ethanol flame. The above two synergic effects, of a sufficient thermal energy and weakly reductive atmosphere, would exclusively lead to the formation of the thermodynamically stable phase, *i.e.*, VO_2(R) (Fig. 7b). The space-confined combustion process presents remarkable convenience, which readily brings the hard-to-access VO_2(R) material into the laboratory.

3.1.2 Using high structural resemblance precursors in the fast and low-temperature heat transformation into VO_2(M). Understanding the correlation of the atomic structure between other vanadium oxides and VO_2(R) provides guidelines for the synthesis of VO_2(M)/VO_2(R). At first, we paid our attention to the new nsutite-type VO_2.[74] It has the random intergrowth structure of VO_2(R) and ramsdellite-type VO_2,[75] which structurally resembles VO_2(R). The calculated total energy has a tendency to be lowered with the increment of the rutile component as shown in Fig. 8a, providing the driving force for the phase conversion from nsutite-type to VO_2(R). As expected, heating the nsutite-state VO_2 at 350 °C under an inert-gas atmosphere produces VO_2(R) as a consequence of temperature-induced movement of the vanadium atoms, as shown in Fig. 8b. However, the structural conversion from nsutite is not an easy task. Only when three layers of vanadium atoms take unified action can the rutile structure be produced, which provides a higher reaction barrier in this case. As a consequence, the VO_2(R) can be obtained by heating the nsutite-state at a relatively lower temperature, but it still needs a relatively long reaction time, of about 6 h.[74]

Alternatively, the highly internal lattice match of the V–O frameworks between paramontroseite and the rutile structure inspired us to develop an ultrafast transformation pathway to VO_2(R). As shown in Fig. 9, both paramontroseite VO_2 and VO_2(R) possess a slightly-distorted hexagonal close packed (hcp) lattice of oxygen atoms, with similar atom arrangements. For these two kinds of vanadium dioxides, different arrangement positions of the V^{4+} atoms determine the phase type of paramontroseite VO_2 and VO_2(R) due to the given similar oxygen framework.[76] Careful observation of the structural lattices can find that the slight movement of V^{4+} ions in paramontroseite into the neighboring vacancies exclusively leads to the crystal structure of VO_2(R). Guided by the structural analysis results, the developed solid-state transformation pathway from paramontroseite to VO_2(R) successfully realized the ultrafast (both steps were complete within 60 seconds) transformation into the desired VO_2(M) phase.[65] The ultrafast transformation methodology provides a facile and inexpensive route to the hard-to-access VO_2(M).

3.1.3 Solid-state reaction pathway to one-dimensional VO_2(M) nanostructures. One-dimensional VO_2(M) nanostructures, with a small radial dimension while retaining wire-like connectivity, represent a particularly attractive class of materials owing to their structural versatility as well as their unique chemical and physical properties.[77] Also, the confined dimensionality, with a size smaller than the domain size in VO_2, helps to reveal intrinsic physicochemical properties, of which one-dimensional VO_2(M) nanostructures, including nanowires/nanobeams, *etc.*, have received considerable attention. During the past several years, great progress has been made in controlling the synthesis of VO_2(M) nanowires and its growth orientation, which entails widely fascinating applications that are built by the one-dimensional nanowires/nanobeams.

The as-reported cases of the VO_2(M) nanowires were dominantly performed using the vapor transport methods, in which a lower gas pressure was usually used to promote the vapor formation from the starting materials. In the early 2005, Prof. Park reported the first available methodology to achieve the single-crystal vanadium dioxide nanowires.[78] In their case, under a lower gas pressure of 12–13 Torr, bulk VO_2 powders were introduced as the starting materials, and the reaction product was collected on a substrate downstream from the flow gas. They found that the formed nanowire density greatly depended on the choice of substrate. On the SiO_2 substrate, the grown nanowires were longer but with low density; for the Si_3N_4 substrate, the greatest nanowire density was achieved. A detailed formation mechanism of vanadium dioxides were

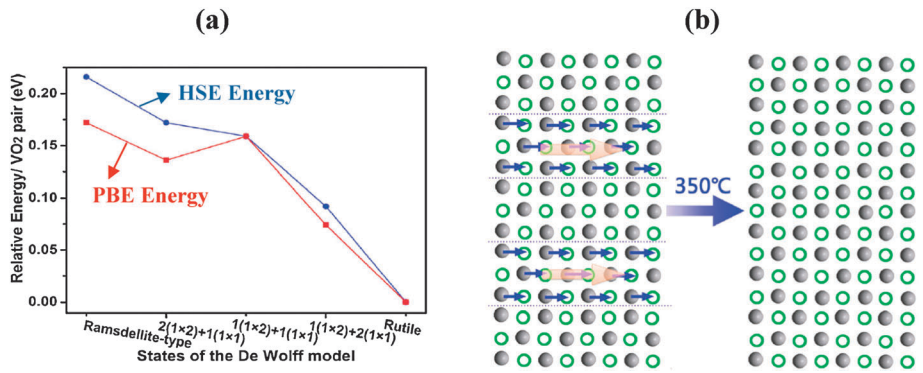

Fig. 8 Using new-state nsutite-type VO_2 as a high structural resemblance precursor towards VO_2(M). (a) Calculated formation energies of the states from the De Wolff model as a function of the relative amount of single chain (P_r) (probability of 1 × 1 tunnel). (b) Schematic illustration of the phase conversion from new-state nsutite-type VO_2 to final VO_2(R). (Adapted with permission from ref. 74, Copyright 2012 Royal Society of Chemistry.)

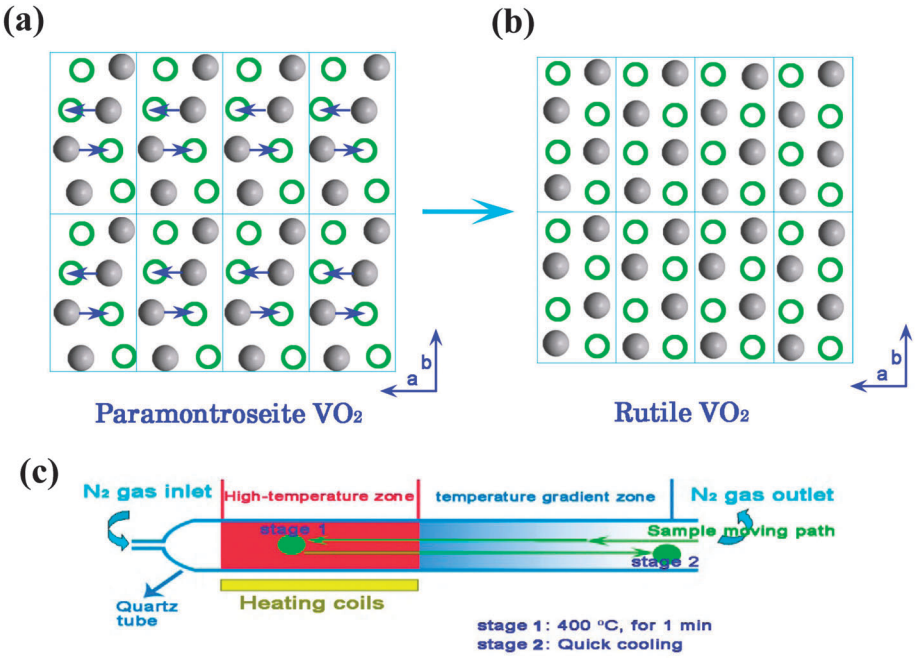

Fig. 9 Using paramontroseite as a high structural resemblance precursor towards VO_2(M) within a very short time of only 60 s. Schematic representation of the structures of precursor paramontroseite VO_2 (a) and VO_2(R) (b), in which only the V^{4+} atoms (represented by filled cycles) and vacant octahedral sites (represented by empty circles) are presented. (c) Schematic illustration of the synthetic procedure for the ultrafast transformation into VO_2(M). (Adapted with permission from ref. 65, Copyright 2011 American Chemical Society.)

lacking in this work, however, they suggested a growth model of the diffusion-based vapor-solid mechanism responsible for the VO_2(M) nanowire growth.[79] Along with the vapor transport methodology, different starting materials such as the V_2O_5 and VO_2(B) have also successfully produced the VO_2 nanobelts.[80,81]

Soon afterwards, Stucky and Wodtke also reported a new growth mechanism for the formation of VO_2 nanowires from supercooled liquid nanodroplets.[82] As is known, for vanadium oxides, V_2O_5 has a very low melting point of T_M = 690 °C, while the melting point of VO_2(M) is rather high, up to T_M = 1967 °C.[83] In this case, using VO_2 powder sample as the starting material and a controlled reaction temperature of 550 °C–650 °C, supercooled V_2O_5 liquid nanodroplets form on the substrate downstream as the growth sites for VO_2(M) nanowires (as shown in Fig. 10). Under mild reducing conditions, the VO_2 nanowire would gradually grow from the supercooled liquid nanodroplets by consuming the liquid drops. Of note, the simple growth from the supercooled liquid nanodroplets shows a certain degree of generality for the growth of nanowires, such as MoO_2, MoO_3, RuO_2, Fe_3O_4, *etc.*

Applying a similar vapor phase transportation method with other appropriate substrates, provides multiple opportunities to control the growth and orientation of vanadium dioxide nanowires.[84] Precise control over the orientation of the vanadium dioxide nanowires is beginning to emerge at the current stage, however, further work is still needed to control the position and orientation for integrating the 1D nanowires into a designed system. Due to the heteroepitaxial interface between VO_2(R) and the sapphire planes,[85] the single crystalline VO_2

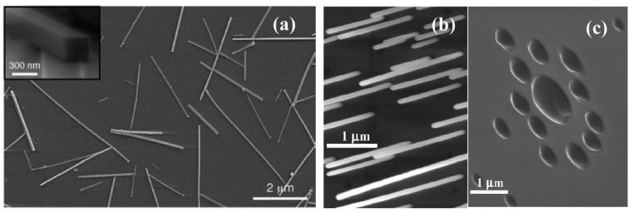

Fig. 10 Vapour-transport method to VO_2 nanowires: (a) SEM image of the VO_2 nanowires as grown on a Si_3N_4 substrate. (Adapted with permission from ref. 72, Copyright 2011 American Chemical Society.) (b–c) Using the supercooled liquid droplets to grow VO_2 nanowires: (b) VO_2 nanowires on r-cut sapphire, where nanowires form an angle with respect to the basal r-cut sapphire. (c) A clear image of droplet-like structures under a tilted angle, indicating the active growth sites for the nanowires. (Adapted with permission from ref. 82, Copyright 2011 American Chemical Society.)

nanowires could be epitaxially grown along the [100] direction with a unique growth orientation relationship with respect to the planes of the sapphire substrates. High structural correlations exist between the VO_2(M) and the sapphire substrates, both of which have the close-packed arrangements of oxygen atoms for (010) VO_2 and (0001) sapphire.[86,87] Thus, the vapor reactants absorb at the appropriate sites and afterwards the vanadium cations arrange in the interstices of the close-packed oxygen network, forming enlarged areas of the $(0\bar{1}1)$ and (011) facets as the low-energy surface, growing along the [100] direction. Of note, for the VO_2(R) structure, the preferred growth direction is usually along the [100] direction. In the meantime, minimization of the surface energy plays a vital role in the

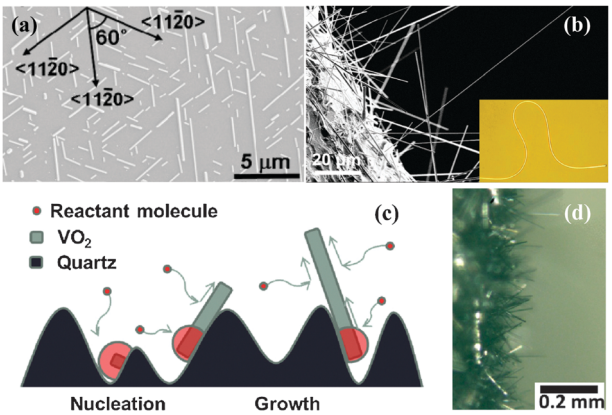

Fig. 11 (a) A typical SEM image of VO_2 nanowires grown laterally along the three equivalent $\langle 11\bar{2}0 \rangle$ directions of sapphire. (Adapted with permission from ref. 84, Copyright 2007 American Chemical Society.) (b) Scanning electron microscopy image of a VO_2 beam grown vertically on the substructure (insert: optical image of the ultra-flexible nanobeams). (Adapted with permission from ref. 88, Copyright 2010 Wiley-VCH Verlag GmbH & Co.) (c) Proposed growth mechanism of free-standing VO_2 MNWs on rough quartz substrates. (d) Optical image taken from the side view showing free-standing VO_2. (Adapted with permission from ref. 89, Copyright 2012 American Institute of Physics).

formation of nanowires and their orientation. Therefore, epitaxial growth leads to precise control over the position and orientation of vanadium dioxides on substrates. The growth orientation directions of the VO_2 nanowires are affected by the selected crystallographic planes of the sapphire substrates, c-cut and a-cut sapphire substrates lead to a cross-section with angles of 60°/120° and parallel alignment, respectively (Fig. 11a). In this regard, the lowest surface energy and the crystallographic lattice match determine the growth direction and the nanowire orientation on the substrates.

Free-standing VO_2 nanowires, that can free the strain within a one-dimensional structure, have also received considerable interest for device fabrication. Wang *et al.* developed a modified physical vapor deposition method to prepare single-crystal vanadium dioxide nanobeams,[88] in which the substrate was tilted at a specific angle with the gas flow, and then the nanowires with lengths up to a hundred micrometers were obtained at the edge of the substrate (Fig. 11b). In their case, the nanowires stick out of the substrate, which were very easy to be taken down from the substrate to obtain free-standing nanowires. Recent progress has been made for achieving free-standing VO_2 nanowires by Wu *et al.*[89] By using a rough-surface quartz as the substrate (Fig. 11c–d) to guide the nanowire growth orientation, single-crystalline, free-standing, ultra-long, and ultra-dense VO_2 micro/nanowires were achieved *via* a simple thermal evaporation process. The as-obtained free-standing VO_2 nanowires have more benefits, as they can be easily harvested and transferred for further device construction.

As for the growth and assembly of VO_2 nanowires, nanowire orientation over a large area, with highly ordered and exact growth positions, is needed for providing the building blocks for integrated devices. Therefore, much effort should be made in the near future for developing more facile material preparation methods and new assembly routes for given orientations.

3.2 New solution-based pathway to VO_2(M) with MIT behavior

Controlling the solution-based synthesis of VO_2(R) represents a great challenge, and even up to date there are only a few available routes reported to successfully synthesize VO_2(R), although it could be chemically stable in hydrothermal or solvothermal conditions.[90] In fact, the solution synthesis of VO_2(M) would offer advantages, such as functional modification of the correlated solids with functional molecules/groups to utilize and understand the e–e correlations in solids for further applications. However, the direct solution synthesis of vanadium oxides without the post heat-treatment usually leads to the formation of other kinds of crystal polymorphs of vanadium dioxides, such as VO_2(A) and VO_2(B), *etc.*, rather than the most thermodynamically stable rutile phase VO_2.[91] For example, Li *et al.*[92] reported forming high quality VO_2(B) nanobelts through the solution treatment of vanadium-including precursors of ammonium metavanadate (V^{5+}). The difficulty associated with the formation of VO_2(R) is strongly related to the chemical environment of the vanadium ions in aqueous conditions. Thankfully, the VO_2(R) is certainly stable under solution conditions, even under solvothermal conditions in a relatively higher reaction temperature. Banerjee *et al.* reported the formation of VO_2(M) nanostructures by the hydrothermal post-treatment of VO_2(M) commercial powders at reaction temperatures of up to 210 °C.[93]

An alternative way to achieve VO_2(R) under solution conditions relies on the incorporation of other heterogeneous ions to stabilize the rutile structure. When using other rutile transition-metal dioxides as the structural matrix, $VTiO_4$ (rutile $VO_2 \cdot TiO_2$), $VTaO_4$ (rutile $VO_2 \cdot TaO_2$), *etc.*, could be easily achieved under appropriate conditions.[94] With the participation of heterogeneous W ions, VO_2(R) nanostructures could form under the solution reaction conditions.[95] In this case, the partial substitution of V atoms with larger W atoms triggers the distortion of the VO_6 octahedra, enabling the structural transition from VO_2(B) to VO_2(R) under hydrothermal conditions. Even so, synthesis of pure vanadium dioxides under solution conditions is still a practically difficult problem.

Structural analysis provides an important clue regarding the practical difficulty of the formation of VO_2(R) in solution reaction conditions. As is known, the formation of the rutile structure in transition-metal dioxides MO_2 (M = Ti, V, Sn, Pb, *etc.*) strongly depends on the atomic structural characteristics in solution conditions. In a typical rutile structure, the MO_6 octahedra share edges along the *c*-axis direction and corners in the *a*–*b* planes. To assemble a rutile structure, the six-coordinated octahedra actually act as building units, in which the way the octahedra units assemble is responsible for rutile structure.[96,97] Compared with other vanadium oxide polymorphs, the rutile structure possesses special characteristics—less edge-sharing but more vertex-sharing octahedra,[98] and thus it provides a vital clue; obtaining detached MO_6 octahedra

and avoiding an excess edge-sharing structure seems essential for forming the rutile structure.[99] Taking rutile TiO_2 as a reference example, the acid conditions could effectively achieve the detached TiO_6 octahedra or their small clusters to targetly form the rutile phase.[100] Inspired by the above analysis, the acid solution conditions is essential for achieving the detached VO_6 octahedra and the subsequent formation of VO_2(R). For vanadium, new challenge arises from the higher valence states of the vanadium ions. Of note, the high valence state of V^{4+} and V^{5+} in the solution conditions have a greater ability to combine with more oxygen atoms and form condensed polyvanadate structures, which is due to the strong electrostatic forces between the high-valent ions with oxygen anions.[101] This represents the realistic difficulty in the formation of VO_2(M) from V^{5+} and V^{4+} precursors due to the significant lack of detached VO_6 octahedra as the building units for the formation of the rutile structure. As a matter of fact, there are numerous studies in the literature showing that no VO_2(R) phase appears when starting from V^{4+} and V^{5+} precursors.[102] From this point of view, reactants with a lower valence-state provide a greater possibility of forming the isolated V^{3+} ions with weak electrostatic attraction forces, which then facilitates the formation of detached VO_6 octahedra under the acid solution conditions to finally achieve VO_2(R).

As expected, the controlled oxidizing the V(III) precursor of $V(OH)_2NH_2$ in the dilute HNO_3 solutions indeed realized the formation of VO_2(M) nanorods (Fig. 12a).[103] In this case, the reactant $V(OH)_2NH_2$ provides isolated V^{3+} ions, and HNO_3 provides the acid solution conditions and oxidizing effects. Therefore, the hydrothermal synthetic conditions provide a way to directly form VO_2(R), while the nature of the nanorod outlook originates from the way the atoms are packed in the crystal structure (Fig. 12b). Of note, the a_M-axis direction growth of VO_2(M) is just the c_R-axis direction in the VO_2(R) structure. For the rutile structure, it has a tetragonal system with the space group of *P*42/*mnm*, with obvious differences in the *c*-axis and *a*/*b*-axis between the atomic crystal lattice. In effect, the *a*–*c* plane clearly exhibits the presence of octahedra infinite chains along the *c*-axis, and a tunnel structure is presented along the *a*-axis extended directions, clearly showing the stacking density difference between the *c*-axis and the *a*-/*b*-axis in the rutile structure.

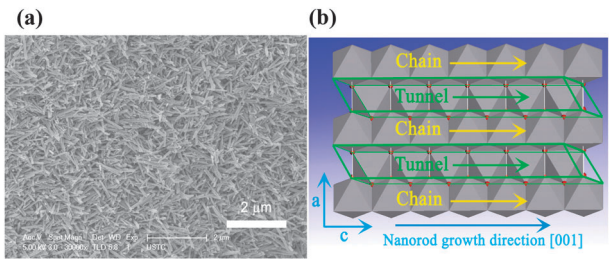

Fig. 12 Solution synthesis route to VO_2(M) nanorods: (a) FESEM images of the VO_2(M) product obtained from the solution-based synthetic methodology. (b) The polyhedra-type supercell structure of VO_2(R), showing the different stacking densities along the *a*-axis and *c*-axis. (Adapted with permission from ref. 103, Copyright 2011 Royal Society of Chemistry.)

The obtained nanorod morphology in our case is actually the outward embodiment of the internal crystal structure.

Intriguingly, recent reports have reveal that the hydrolyzed precipitate of VO^{2+} with hydrazine also produced VO_2(M). In this case, hydrazine also acted as the reducing reagent to reduce the vanadium ion to V(III), which also ensures the formation of VO_2(M).[104]

4. Chemical synthesis of new vanadium oxides with unique electrical properties

Precisely controlling the atomic structures of vanadium oxides in a desired manner would promote the investigation of the effects of electron–electron correlations on the physicochemical properties. The presence of rich coordination-style configurations forms numerous and varied vanadium-oxide frameworks; also, vanadium atoms have various valence states (from +2 to +5).[105] The various atom-stacking styles form the hundreds of crystal structures of vanadium oxides,[106,107] which provides the material foundation for understanding the interplay between the properties and the atomic crystal structures. However, controlling the vanadium oxide structures is not an easy task, except for the V^{5+} oxides. For the vanadium element with the highest valence state (V^{5+}), there is only one material phase with an orthorhombic crystal system.[108] As long as the reaction temperature is high enough with sufficiently provided oxygen, orthorhombic V_2O_5 would be exclusively formed.[109] As for the lower valence states of +4, more than ten kinds of V^{4+} oxide phases have been reported, arising from the different assembly styles of various V–O units.[110] It is hard to synthesize V^{4+} oxides with a desired structure. However, only very limited V^{3+} phase kinds have been reported. For the V^{3+} hydroxides of VOOH, only three phases of montroseite VOOH,[111] orthorhombic VOOH with *Pbnm* space group,[112] and orthorhombic VOOH with an uncertain structure.[113] In this regard, the limited phase kinds of V^{3+} oxides suggest the presence of research room for pursuing the new structural configurations with the purpose of investigating their potential properties.

From this point of view, low valent vanadium oxides provide new alternatives for designing new structural characteristics with potential functions. On the one hand, the development of new synthetic methodologies towards the known hard-to-access phases, for example, the mineral phases of vanadium oxides, provides appropriate structural systems for investigating the physicochemical properties. In this regard, only successfully accomplishing the chemical synthesis of these structures entails the possibility for systematical investigation of their material properties based on the given structures. On the other hand, pursuing new structures of vanadium oxides with particular characteristics also provides alternative ways to investigate the material properties from the electron–electron correlation effects in vanadium oxides. Obviously, the new structures with the desired atomic arrangements would provide a material platform for the relevant investigations. Recently, some progress in the design of new vanadium oxides *via*

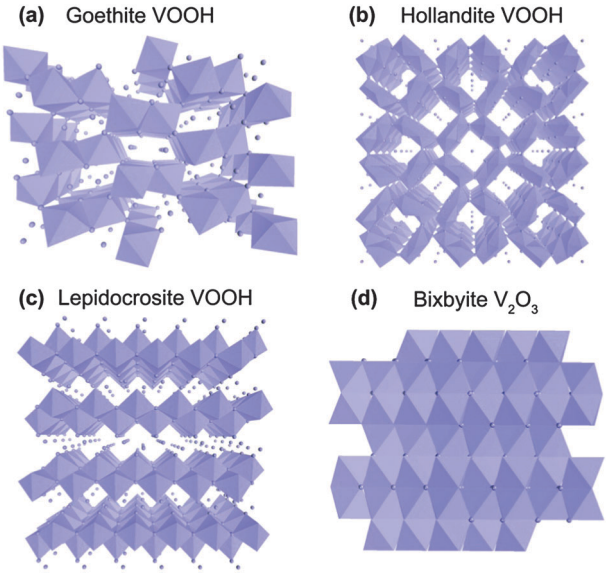

Fig. 13 Recently discovered new-phased vanadium oxides.

chemical reaction routes has been successfully established for both the new chemical routes to known hard-to-access vanadium oxides and to the new phased vanadium oxides, especially for the synthetic mineral phases (such as haggite, paramontroseite) and the new-phased structures (for new-phased goethite VOOH, hollandite VOOH and lepidocrocite VOOH, and cubic bixbyite structure V_2O_3, *etc.*) (Fig. 13).

4.1 Mineral phases of vanadium oxides

For vanadium oxides, there are numerous vanadium oxide mineral structures that have been known over the past century. For example, paramontroseite and haggite were two typical mineral structures, both of which were discovered from the Colorado Plateaus region in the 1950s and the structural models have been proposed since their discoveries.[114,115] However, since then, these mineral phases have been severely neglected. Synthetic paramontroseite and haggite structures were first obtained by our controlled chemical reaction routes.[116,117] These two structures both have infinite V^{4+}–V^{4+} atomic chains in their internal crystal structures, providing intriguing models for investigating their electron–electron correlations. As is known, the electron configuration of vanadium is $3d^34s^2$, thus the V^{4+} ions in both paramontroseite VO_2 and haggite would have single $3d^1$ electrons. For paramontroseite, the presence of infinite chains with the nearest V^{4+}–V^{4+} distance of 0.293 nm ($<R_c$) enables the $3d^1$ electrons to be shared by all of the V–V atom chains along the *c*-axis. Thus, paramontroseite possesses promising electrical conducting properties, showing an electric resistivity of 9.8×10^{-3} Ω m at room temperature. For the haggite structure, infinite V^{4+}–V^{4+} chains along the *b*-axis are present with the nearest V–V distance of 0.299 nm, which is larger than that of the critical V–V distance (R_c = 0.294 nm), and thus haggite behaves as a semiconductor with a relatively higher resistance of 55.40 Ωm. Due to the presence of infinite chains, similar to that of VO_2(R) with fully-reversible electrical switching properties, haggite also exhibits a switchable electrical behavior of a semiconducting-to-insulating transition.[117]

4.2 New vanadium oxide structures

Transition metal oxides possess rich structure types, among which many crystals are in the same kind of structure but with diverse elements. For example, the rutile structure widely exists in titanium dioxides, tin dioxides, lead dioxides, *etc.*[118] Another notable case is the wurtzite crystal structure, named after the mineral wurtzite, which is widely found in various binary compounds with a hexagonal crystal system, covering AgI, ZnO, CdS, CdSe, α-SiC, GaN, AlN and many other semiconductors.[119,120] The same kind of structure usually has a high resemblance in atomic positions and symmetries but with different kinds of elements, giving the direct representation by the high similarity of the XRD patterns.[121] In this regard, the XRD technique plays a crucial role in the search for new important structures. Several preceding results have shown the effective ways it has been applied to finding new structures. For example, the XRD pattern of $AgInSe_2$ nanorods, formed by the thermolysis of $[(PPh_3)_2AgIn(SeC\{O\}Ph)_4]$, does not match any of the patterns for the reported $AgInSe_2$ structures, but highly resembles the XRD pattern of orthorhombic $AgInS_2$ with a certain degree of 2θ position shifting.[122] Moreover, using the $AnInS_2$ cell parameters as a reference, the calculated new cell parameters of $AgInSe_2$ is more consistent with the experimental results. Based on the combined analysis results, new-phased $AgInSe_2$ with a previously unknown orthorhombic phase that is isostructural to $AgInS_2$ has been found. More recently, unprecedented hexagonal wurtzite MnO has been uncovered *via* the thermal decomposition of $Mn(acac)_2$.[123] In this case, employing the single line fitting technique to extract the contribution of the crystalline component reveals the highly resemblance of the as-obtained pattern with other kinds of wurtzite transition metal oxides,[124] suggesting the new-phased MnO structure.

The discovery of new-phased vanadium oxide materials strongly depends on the close resemblance of the crystal structure, which is isostructural to other transition metal oxides, especially for iron oxides. It is very interesting that there are strong correlations between iron oxides and vanadium oxides, perhaps due to the similar ionic radius of vanadium (64 pm for V^{3+} and 58 pm for V^{4+}) and that of iron (64.5 pm for Fe^{3+}).[125] That is to say, all the crystal forms of the new vanadium oxides/hydroxides are already well-known in other transition metal oxides, especially in iron oxides. The found crystal structures of the new vanadium oxides are just isostructural to the known forms in other metal oxides.

4.2.1 New-phased VOOH family members. By utilization of this strategy, serial VOOH new phases, including lepidocrocite, goethite, and hollandite VOOH were found. Shown in Table 1 are the crystal forms of goethite, hollandite, lepidocrocite, and feroxyhyte in traditional metal oxides which are already well-known; however, the forms in VOOH have not been well understood.

Table 1 Crystal information of the newly discovered vanadium hydroxide, along with the crystal information of the iron hydroxides for comparison.

Iron hydroxides			Vanadium hydroxides	
Formula	Crystal system	Mineral name	Phase existence	Ref.
α-FeOOH	Orthorhombic	Goethite	New phased	65
β-FeOOH	Tetragonal	Hollandite	New phased	131
γ-FeOOH	Orthorhombic	Lepidocrocite	New phased	126
δ-FeOOH	Hexagonal	Feroxyhyte	Non-existant	None

Lepidocrocite VOOH is the first case of a new-phased material structure.[126] The corresponding XRD pattern provides structural information. The XRD patterns of vanadium oxides, formed by reducing a NH_4VS_3 suspension solution with $N_2H_4{\cdot}H_2O$, could not be assigned into any XRD patterns shown in previous reports, but it is almost identical to lepidocrocite FeOOH with orthorhombic structure. From a structural point of view, the structure of the as-obtained vanadium oxides is isostructural to the orthorhombic lepidocrocite γ-FeOOH.[127] With the benefit of other combined characterizations, the new-phased lepidocrocite VOOH structure can be well unravelled. The crystal structure of the new lepidocrocite VOOH is completely different from the known VOOH phases, in which the corrugated ribbons of edge-sharing VO_6 octahedra, that are one and a half octahedra in width, share corners forming lamellar sheet structures. In this structure, the layered vanadium oxide octahedra bonded by hydrogen bonding *via* hydroxide layers, causing the formation of nanosheet units due to exemplifying the highly anisotropic internal crystal structure.[128]

Another new-phased V(III) hydroxide VOOH, hollandite, was also obtained owing to the discovered V(III) precursor $V(OH)_2NH_2$. It is known that its material phases still originate from the peak analogue in the XRD pattern. The hollandite-type VOOH is also the unprecedented material phase, although the hollandite structure has been widely known in other transition metal oxides such as α-MnO_2, K_xTiO_2, *etc.*[129,130] In the hollandite structure, the octahedra of the double chains share corners with adjacent double chains to construct an infinite 2 × 2 tunnel structure. Using the F^- as the structural stabilizer for the large 2 × 2 tunnel structure, reaction of the V(III) precursor $V(OH)_2NH_2$ in an aqueous solution of ionic liquid [BMIM][BF_4] leads to the formation of hollandite VOOH.[131] In this case, the corresponding XRD pattern also could not be indexed to any standard XRD patterns among the JCPDS cards or previously reported vanadium-including materials. However, it is identical to that of hollandite-type β-FeOOH with a tetragonal system, as shown in Fig. 14a. That is to say, the crystal structure of this material is isostructural with that of tetragonal hollandite β-FeOOH. The new-phased hollandite-type VOOH is particularly attractive due to the presence of infinitely linear V^{3+}–V^{3+} chains in its internal crystal lattice. The infinite V atom chains lead to the electrical-switching properties, exhibiting the representative semiconductor–insulator transition behavior.

New-phased goethite-VOOH was prepared by the reaction of sodium orthovanadate ($Na_3VO_4{\cdot}12H_2O$) with thioacetamide (TAA).[67] The XRD pattern of the vanadium oxides could be readily indexed to goethite-type FeOOH with an orthorhombic system, and it cannot be indexed to any kind of vanadium-including structure. Also, the simulated XRD pattern of the goethite VOOH crystal cell is identical to the experimental one (Fig. 14b), providing direct evidence of the presence of the goethite VOOH structure. The new-phased goethite VOOH has a regular 1 × 2 tunnel structure, similar to the paramontroseite VO_2 structure.

4.2.2 New-phased V_2O_3 family member. Compared with the abundant phase kinds of Fe_2O_3 and Al_2O_3, no other vanadium sesquioxides (V_2O_3) exist except for the V_2O_3 phase with a rhombohedral corundum-type structure at room temperature. The sole V_2O_3 phase behaves with a MIT, with the structural phase transition depending on the environmental temperature.[132] At room temperature, this phase crystallizes

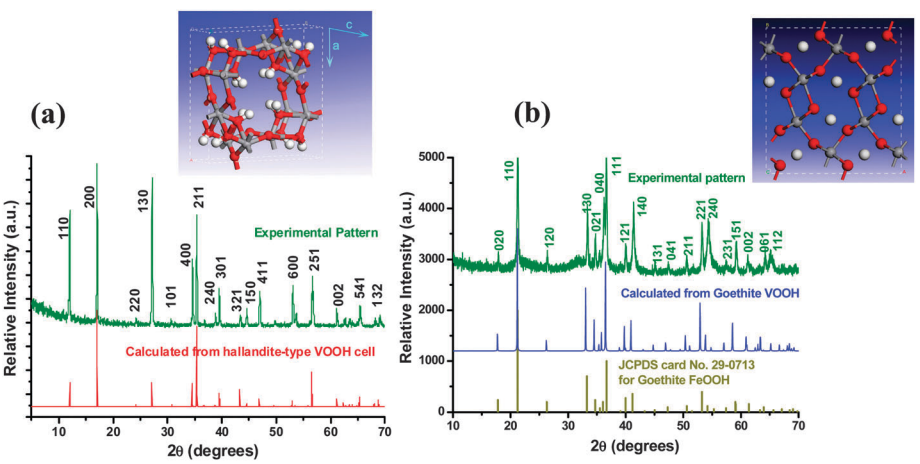

Fig. 14 The experimental XRD pattern and calculated XRD pattern achieved from the crystal cell, as well as the unit cell of (a) new-phased hollandite-type VOOH. (Adapted with permission from ref. 131, Copyright 2010 Royal Society of Chemistry) (b) New-phased goethite VOOH. (Adapted with permission from ref. 65, Copyright 2011 American Chemical Society.)

with a rhombohedral corundum-type structure, exhibiting paramagnetic and metallic behavior. Upon depressing the sample temperature to <170 K, a monoclinic polymorph appears after a structural phase transition process.[132]

Uncovering the new-phased cubic bixbyite structure of V_2O_3 represents one notable case. As is known, the bixbyite structure is a mineral phase, widely existing in other various transition metal oxides, such as Fe_2O_3, Mn_2O_3, Sc_2O_3, In_2O_3, *etc.*[133,134] However, this phase of vanadium sesquioxides is significantly lacking. The bixbyite V_2O_3 was initially obtained by annealing vanadyl ethylene glycolate.[135] In this case, structural information is also achieved by analysis of the XRD pattern. The experimental one cannot be directly indexed to any kind of vanadium oxide or the vanadium-including material, revealing the existence of a new phased vanadium oxide. The high resemblance of the XRD pattern confirms that the crystal lattice of the new vanadium oxide is isostructural to the bixbyite structure, which is already well known in other transition metal oxides, such as bixbyite β-Fe_2O_3.[136] Interestingly, the new polymorph can also crystallize in the bixbyite-type structure by controlling the reaction of VF_3, while avoiding oxidation or reduction in the reaction system.[137] It was also revealed that the bixbyite-type V_2O_3 is a metastable phase, and can be structurally transformed into the more thermodynamically stable corundum-type V_2O_3 at $\sim$823 K. The new phased V_2O_3 has a body-centered cubic structure, where 16 formula molecules are in one unit cell and 32 vanadium atoms occupy the two non-equivalent sites in the distorted octahedral lattice voids. In this kind of structure, all the octahedra are interlinked *via* edges. First principle calculations verified the metastability as well as the semiconducting behavior of the cubic bixbyite structure.[138]

Despite the progress made in searching for new V_2O_3 structures, on the account of there being limited phase kinds for reported V_2O_3,[139] there is still much room for discovering new crystal polymorphs in vanadium oxides. For example, there are four known iron(III) oxides (Fe_2O_3), including alpha phase, hematite (α-Fe_2O_3), beta phase, (β-Fe_2O_3), gamma phase, maghemite (γ-Fe_2O_3), and epsilon phase, (ε-Fe_2O_3).[140] For their isostructures of V_2O_3, hitherto only two kinds of the rhombohedral corundum-type and bixbyite-type V_2O_3 have been discovered. The maghemite and epsilon V_2O_3 phases have not been discovered up to now.

The low number of reported vanadium(III) oxide and hydroxide crystallography studies before the recent progresses might be related to the chemical instability of the low valence state vanadium ions, especially V^{3+}. In effect, the V^{3+} precursor is very hard to achieve due to it being too sensitive towards oxidation to the higher valence vanadium oxides. The systematical synthetic routes toward new vanadium oxides with lower valence states gradually discovered a series of new vanadium oxide structures that were previously unknown. A series of new-phased vanadium oxides were discovered owing to the newly founded V^{3+} reactants, based on the V^{3+} being easily controlled under solution conditions and could converted to vanadium hydroxides or oxides in the appropriate reaction systems. The discovery of these new structures in vanadium oxides also exhibits the electrical-switching properties that arise from the electron–electron correlated effect. For example, hollandite-type VOOH has infinite linear V^{3+}–V^{3+} chains in the internal crystal lattice leading to the smart-switching electrical properties. In a word, although the functional applications for these formed new-phased structures are still under investigation, and these new vanadium oxides have brought alternative e–e correlated platforms, they have potential unique electronic properties and even smart switching behaviors.

5. Vanadium oxides with controllable electrical properties bringing energy-related applications

Controlling the structural lattices of vanadium-including materials can effectively influence the electron–electron correlations, bringing about the desired electronic structures, which provides a new effective way to adjust the carrier concentrations and electrical conductivity of a material as schematically described in Fig. 15. As is known, the carrier concentration as well as the electrical conductivity are crucial parameters that could significantly influence the performance in various energy storage and energy conversion applications such as lithium-ion batteries, supercapacitors, and thermoelectrical applications.[141,142] Also, the MIT that arises from the electron–electron correlations in vanadium oxides has shown promising signs for the construction of smart windows; while the accompanying magnetic change on passing through the MIT process, provides an opportunity for using the magnetocaloric effect (MCE) as energy utilization technology.

5.1 Enhanced electrical conductivity *via* regulation of the electron–electron correlations

5.1.1 Conducting vanadium oxides for aqueous-electrolyte rechargeable lithium-ion batteries (AE-RLIBs). Over the past two decades, aqueous-electrolyte rechargeable lithium-ion batteries (AE-RLIBs) are emerging as an important technology for the development of new types of safer and less expensive rechargeable cell systems.[143,144] AE-RLIBs adopt an aqueous-electrolyte (alkaline or neutral) solution as the electrolyte in a lithium-ion battery system, to overcome the practical difficulties for organic electrolytes in RLIBs, which could produce safety problems, such as dense smoke, fire, and even explosions, as well as additional cost.[145] Vanadium oxides were used as the prototype electrode material for the AE-RLIB system, due to their appropriate electrochemical window and chemical voltages for matching the counter electrodes in AE-RLIBs.

As is well accepted, the electronic/ionic conductivity of the activated electrode material is responsible for the kinetic problems associated with LIB systems.[146] Regulating the conductivity of the vanadium oxides provides a feasible way to mitigate the kinetic problems, leading to the improvement of AE-RLIB performances. In this regard, understanding the electron–electron correlation is a new effective way to selectively control the carrier concentration with the desired electrical

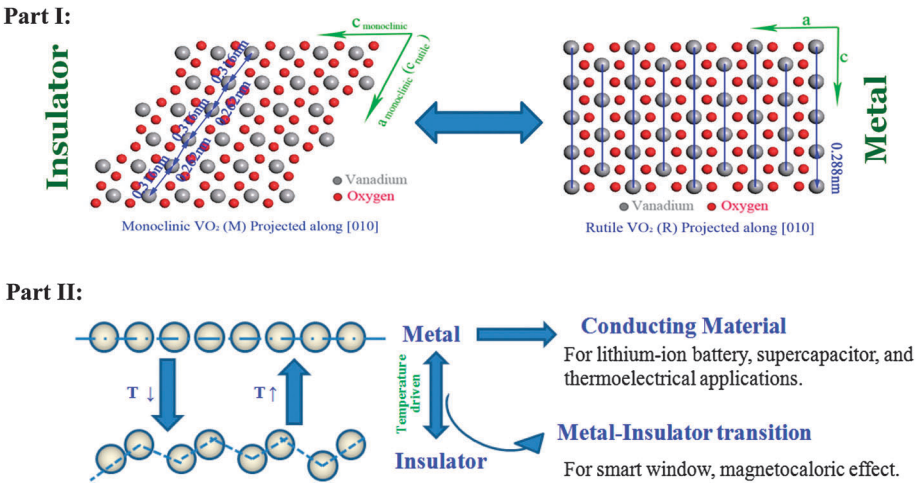

Fig. 15 Schematic illustration of the metal and insulator states by different alignment styles of vanadium atoms in vanadium oxides. Part I: The MIT occurs when the infinite linear vanadium atoms distorted into the zigzag structures driven by the lowering temperatures. Part II: For the vanadium oxides, when all the vanadium atoms were linearly aligned with the overlapping electron cloud of the V 3d, the metal state forms and the conducting vanadium-including materials can be achieved. While linear V atoms were distorted by the temperature, driving the MIT to occur. In this case, the conducting vanadium oxides could find fascinating applications as electrode materials in lithium-ion batteries, supercapacitors, as well as thermoelectrical materials. The MIT of vanadium oxides could be introduced to the construction of smart windows as well as MCEs.

conductivity, which is vital for designing new electrode materials for AE-RLIBs. For vanadium oxides, designing atomic structural lattices with localization/delocalization of the d-orbital electrons provides a way to understand the electrical conducting properties. In a typical vanadium oxide material, the neighboring vanadium–vanadium distance within the critical distance for V^{4+}–V^{4+} or V^{3+}–V^{3+} would enable the electronic cloud sharing for these neighboring V–V atoms. When these chains extend infinitely, the vanadium oxides can conduct with a metallic behavior. In a word, controlling the electron–electron correlation in these systems enables the regulation of the electrical conductivity of vanadium oxide materials.

Paramontroseite VO_2 has a regular tunnel form, in which the double chains of the VO_6 octahedra are linked at the corners with each other in turn to form tunnels with 1×2 octahedra, as shown in Fig. 16a. In this structure, infinite chains are present in paramontroseite VO_2 along the *c*-axis with a nearest V–V distance of 0.293 nm, which is smaller than the critical distance

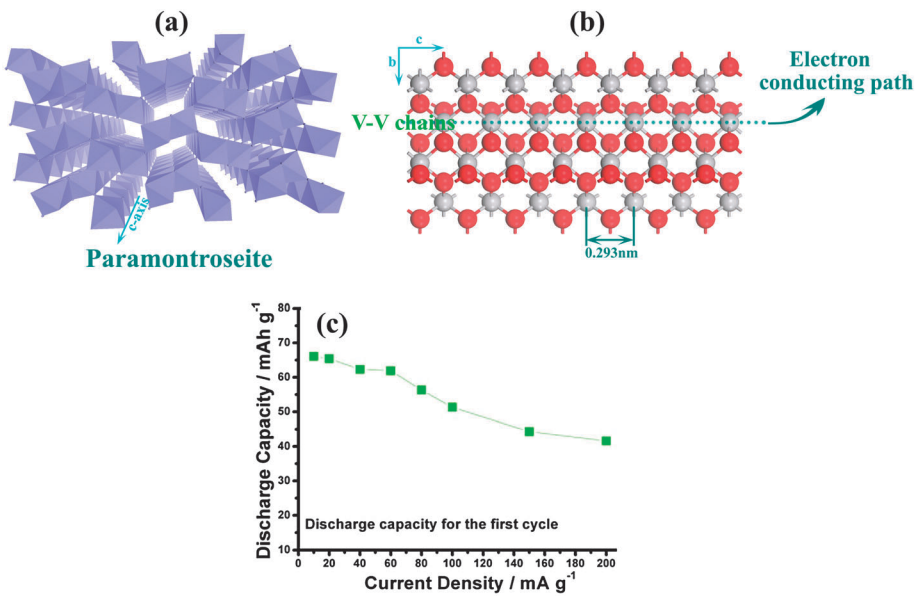

Fig. 16 Conducting paramontroseite for aqueous LIB applications. (a) Super cell structure of paramontroseite VO_2. (b) Atomic illustration of paramontroseite VO_2, in which the infinite linear V^{4+} atoms act as the electron conducting path. In this case, the electron–electron correlations of vanadium atoms produces the conducting characteristics in paramontroseite. (c) The conducting paramontroseite characteristics provides the possibilty for excellent aqueous LIB applications under high current density conditions. (Adapted with permission from ref. 116, Copyright 2008 Royal Society of Chemistry.)

(0.294 nm) for V^{4+}–V^{4+}.[147] The smaller value enables the sharing of d-orbital electrons by the infinite V–V chains along the paramontroseite *c*-axis, and the paramontroseite could then act with a metallic behavior (Fig. 16b). As expected, the electrical conductivity for paramontroseite is found to be 1.02 S cm^{-1} at room temperature. The conducting paramontroseite is expected to facilitate the intercalation/deintercalation of Li^+ ions owing to its high conductivity. Our experiments reveal that the as-established aqueous-electrolyte rechargeable lithium-ion battery based on paramontroseite VO_2 indeed exhibits an enhanced AE-RLIB performance for higher energy density, with the first discharge capacity reaching 61.9 mA h g^{-1} (Fig. 16c) and high output voltages of 1.3–1.6 V and 1.0–1.2 V. Paramontroseite, as an electrode material, also provides good stability under higher current density conditions, in which the high-rate performance is due to the mitigation of kinetic limitations by the high electrical conductivity of the paramontroseite VO_2.[148]

Vanadium sesquioxide (V_2O_3) is generally considered as the classical example of a Mott-Hubbard MIT.[149] V_2O_3 undergoes a striking MIT at 150 K, marked by a jump in the resistivity by seven orders of magnitude and an antiferromagnetic ordering of spins. At temperatures above 150 K, a high-temperature paramagnetic V_2O_3 phase exists with a corundum crystal structure that exhibits metallic behavior. The rhombohedral V_2O_3 has a three-dimensional (3D) vanadium-atom framework where the V 3d electrons could itinerate along the V–V chains due to the neighbor V–V distance, which is smaller than the critical distance, providing it with intrinsic metallic behavior (Fig. 17a). The metallic behavior could be further verified by simulation of its density-of-states (Fig. 17b), where the residual time of the states on the fermi level reveals the metallic behavior. We also designed an aqueous lithium-ion battery electrode using the metallic rhombohedral V_2O_3 as the electrode material.[150] Highly ordered lamellar hybrid nanorods were successfully achieved, consisting of ultrathin V_2O_3 layers (with a thickness of 0.65 nm) that were regularly separated by organic phenylacetate layers (Fig. 17c). The synergic advantages of the metallic behavior and the well-designed morphology features favor the enhanced aqueous LIB performance. Fig. 17d depicted that the first discharge capacity of V_2O_3 with a highly ordered lamellar structure, which was up to 131 mA h g^{-1}. This capacity was remarkably higher than that of other vanadium oxides, such as that for paramontroseite VO_2, as described above. Moreover, the capacity retention of the V_2O_3 lamellar nanorods was as high as 88% after 50 cycles. The coulombic efficiency of the V_2O_3 lamellar nanorods remained at nearly 100%, revealing good reversibility during the long-term charge/discharge tests, and no obvious gas evolution occurred in the cycling voltage region. In a word, the highly ordered lamellar V_2O_3 nanorods displayed a remarkably larger discharge capacity and much superior capacity retention, verifying that the conducting V_2O_3 (with the well-designed morphological characteristics of highly

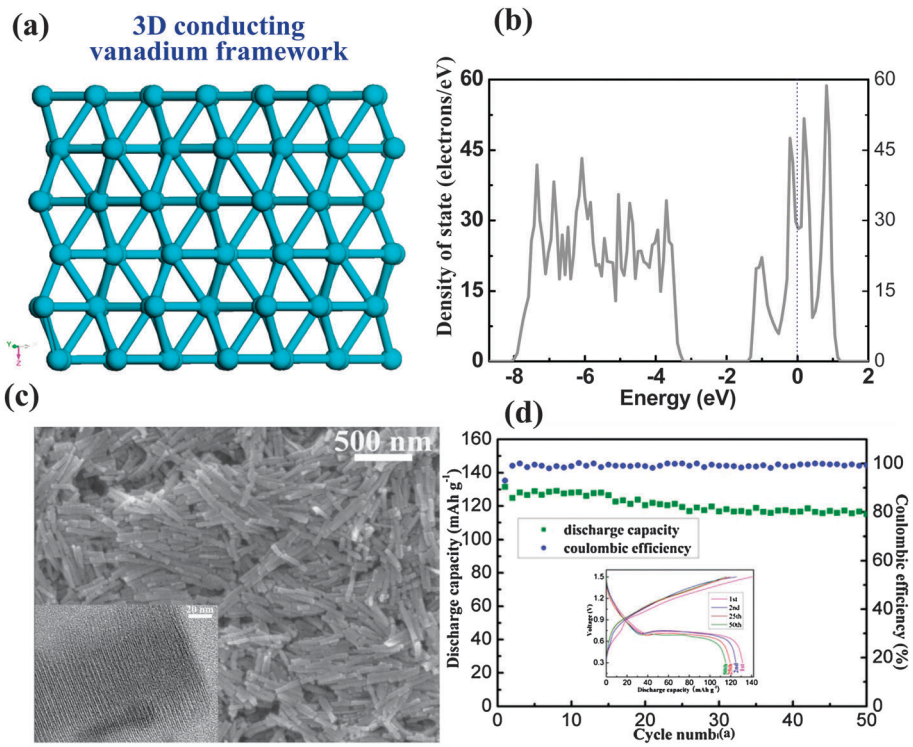

Fig. 17 Conducting rhombohedral V_2O_3 for LIB applications. (a) Three-dimensional (3D) vanadium framework showing the metallic conducting framework for rhombohedral V_2O_3. (b) Total density of states for rhombohedral V_2O_3, clearly revealling its metallic behavior. (c) FE-SEM image of the highly ordered lamellar V_2O_3-based hybrid nanorods, inset is the high magnification TEM image; (d) discharge capacity and coulombic efficiency *versus* cycle number curves, inset is their corresponding charge and discharge curves. (Adapted with permission from ref. 150, Copyright 2011 Elsevier.)

ordered lamellar structures) were responsible for the enhanced performance for the aqueous lithium-ion battery electrodes.

5.1.2 Conducting vanadium disulfide for in-plane supercapacitors. Although VO_2(R) possesses infinite V–V chains with excellent electrical conductivity, the smaller size of the 1 × 1 tunnels in the rutile structure hamper the absorption of protons and cations leading to the unsatisfying supercapacitance. Aside from the one-dimensional electron–electron correlation in the vanadium chains of vanadium oxides, vanadium disulfide (VS_2) is regarded as a prototype model for demonstrating two-dimensional electronic correlations.[151] As a typical family member of TMDs, VS_2 crystals are composed of metal V layers sandwiched between two sulfur layers and are stacked together by weak van der Waals interactions.[152] Theoretical investigations reveal that the monolayered structure of VS_2 has a metallic behavior, in which the density of states (DOS) (see Fig. 18a) resides across the Fermi level with high local DOS values, presenting a promising sign for high microscopic 2D conductivity. Moreover, the weak van der Waals interlayer interactions provides practical feasibility for VS_2 to be exfoliated into ultrathin nanosheets with high surface activity, similar to the exfoliation of graphite into graphene.[153] These results demonstrated that 2D metallicity could be derived from the electron–electron correlations among the in-plane vanadium atoms, resulting in a metallic graphene analogue material of VS_2, which has been experimentally verified as shown in Fig. 18b.

As is known, with regard to the evaluation of electrode material in supercapacitors, the conductivity and specific surface area are two critical factors that determine the supercapacitor performance.[154] Considering the advantages of 2D conducting materials for planar energy storage devices, VS_2 nanosheets with high electric conductivity would be of high interest and of significance for the fabrication of planar supercapacitors, *i.e.*, building two electrodes onto the same plane (or surface), which is newly emerging as a noteworthy and promising candidate for next-generation energy storage devices.[155,156] Practically, supercapacitors with an in-plane configuration can be fabricated as is schematically illustrated in Fig. 18c, in which the two working electrodes are built onto the same plane and the electrolyte ions migrate horizontally, parallel to the substrate surface.[157] As is expected, as shown in Fig. 18d, a specific capacitance of 4760 μF cm^{-2} was realized here in a 150 nm in-plane configuration, of which no obvious degradation was observed even after 1000 charge/discharge cycles, offering a new in-plane supercapacitor with high performance based on quasi-2D materials.[158]

5.2 Applying vanadium dioxides for thermoelectric applications

5.2.1 Enhanced carrier concentrations for thermoelectric properties. As is well known, thermoelectric effects can directly convert waste heat to electric power, with the ability to convert from thermal to electrical energy, behaving as a vital technology

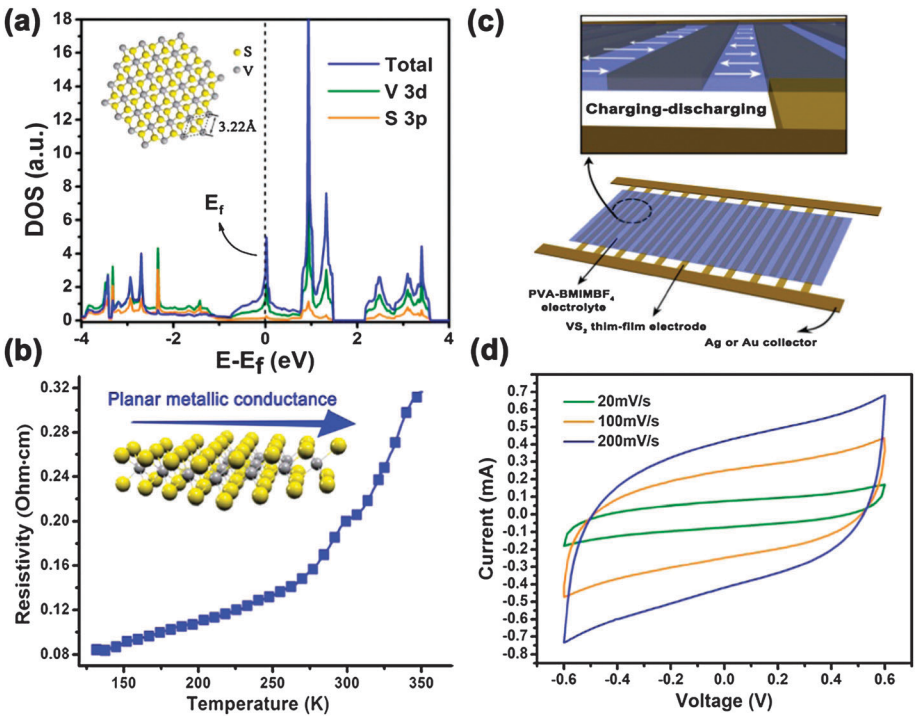

Fig. 18 Conducting 1T VS_2 for in-plane supercapacitor device. (a) DOS diagram for single-layered VS_2 calculated by Heyd–Scuseria–Ernzerhof (HSE) hybrid functional, revealing the 2D metallic nature of the VS_2 single layers. Inset is the *c*-axis projected atomic view of S–V–S, a single layer structural lattice. (b) Temperature dependence of planar resistivity of the VS_2 thin film. Inset is a single layer structural lattice of S–V–S atoms. (c) Top: Planar ion migration pathways for the in-plane supercapacitor; Bottom: Schematic illustration of the in-plane configuration of the as-fabricated supercapacitor. (d) Cyclic voltammetry at different scanning rates of 20, 100, and 200 mV s^{-1}. (Adapted with permission from ref. 158, Copyright 2011 American Chemical Society.)

for energy harvesting.[159] The thermoelectric performance strongly relies on the three well-known thermoelectrical parameters of electrical conductivity (σ), thermoelectric power (S), and thermal conductivity (κ). All three are strongly dependent upon the electronic structure and charge carrier-related properties of the material.[160,161] In this regard, compared with the traditional doping method that is widely used in thermoelectrical materials, the strongly correlated electronic systems provide a new platform for regulating carrier concentration. In correlated material systems, the active control and manipulation of the charge and spin degrees of freedom of electrons or atomic orbital orientations create the expected electronic structure, resulting in the controllable charge carrier related properties and controlled thermoelectric parameters.[162]

Vanadium oxides, especially for the VO_2(M), with the strong e–e correlation effects, could naturally be the right material platform to investigate the effects of e–e correlations on the thermoelectric performances. During the fully-reversible phase-transition process from VO_2(M) to VO_2(R), the orientation change of electron clouds accompanying the structural transformation process could accordingly change the state of electron spin.[163] This process results in the widening/narrowing of the material bandgap to form the insulator of VO_2(M) or metal states of VO_2(R) in one material system. Modulating the electronic correlated effects realized the controlling carrier concentrations, which is vital for thermoelectric performance.

Our group included light H^+ in the exterior environments, such as the 1 × 1 tunnels or crystal surface of VO_2(R) lattices, without structurally distorting the main lattice.[164] In this case, the H^+-including would also contribute additional electrons to the V–O systems, leading to the enhancement of the e–e correlation effects along the infinite linear V–V chains (Fig. 19a). Density functional theory calculations reveals the involvement of H^+ in hydric VO_2(R), which leads to the appearance of some peaks just below the Fermi level (as shown in Fig. 19b), while the orbital without H^+ is an unoccupied one, when considering the extended direction of the infinite V–V chains (c_R-axis). It clearly suggests the enhancement of electron–electron correlation effects along the infinite linear V–V chains. In our case, the enhanced e–e correlation effects would strengthen the electronic orbital overlap of the infinite V–V chains in VO_2(R), which are then harder to break compared to the system without H^+ ions, and thus successfully stabilizing the high-temperature-phase metallic VO_2(R) down into room temperature. By controlling the hydrogen concentrations with gradient hydrogen contents of 3.8‰, 1.3‰, nearly zero, the metallic VO_2(R), semiconducting VO_2(M) and their intermediate states of their mixture were obtained accordingly (Fig. 19c),

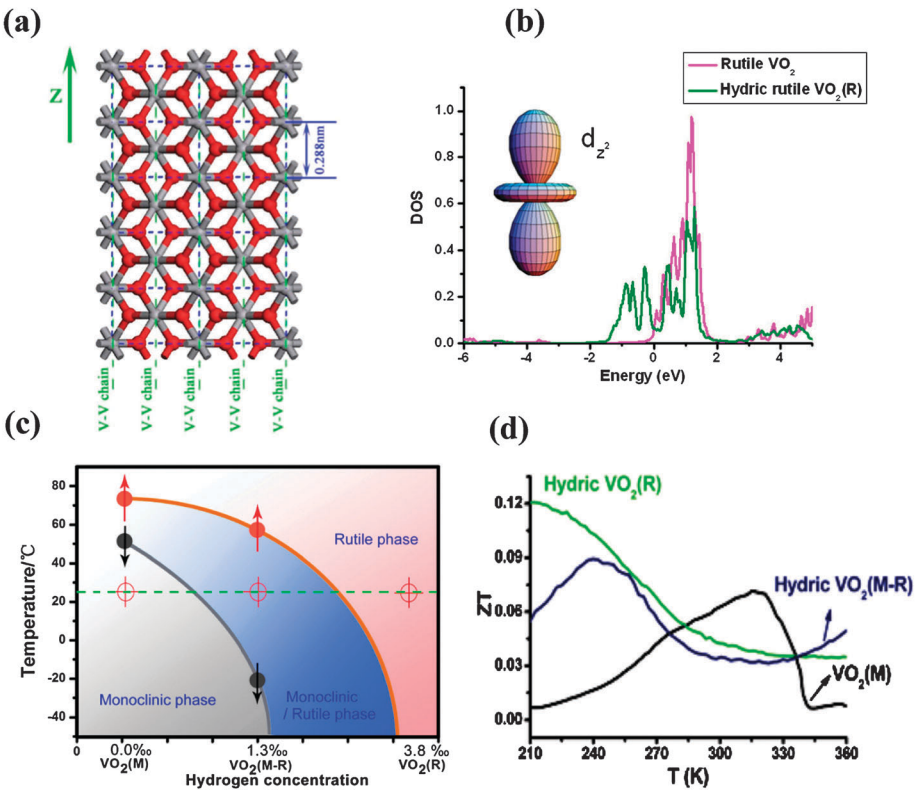

Fig. 19 Hydrogen-incorporation enhances the electron–electron correlations in VO_2(R), leading to the improved thermoelectric performance across a wide working temperature range: (a) atomical illustration of the hydric VO_2(R). (b) Partial DOS of the d_{z^2} orbital of vanadium in hydric VO_2(R), in which the DOS curve crossed the Fermi level at −2 eV, suggesting the enhanced e–e correlation in VO_2(R). (c) Evolution of the transition temperature, T_c, with change in hydrogen concentration, from which it can be seen that at the room temperature, the metallic rutile phase, semiconducting monoclinic phase, and its mixed phase could be obtained respectively, giving >3 orders of magnitude carrier concentration gradients in our case. (d) Temperature dependence of the thermoelectric figure of merit in hydric VO_2(R), and that of VO_2(M), hydric VO_2(M–R) is for comparison. (Adapted with permission from ref. 164, Copyright 2011 American Chemical Society.)

bringing larger than three orders of magnitude carrier concentration gradients, providing an ideal material model to investigate thermoelectric effects. Our figure of merit behavior in Fig. 19d shows that the thermoelectric devices have a wide range of working temperatures. In detail, the hydric VO_2(R) achieves a high ZT maximum value of 0.12 at the low temperature of 210.0 K, which is higher than that for hydric VO_2(R–M) (0.089, 240.4 K) and VO_2(M) (0.071, 316.6 K). Therefore, we could successfully picture a new physical scenario: that regulation of the e–e correlation is an effective model for selectively controlling the metallic and semiconducting states, bringing larger carrier concentrations gradients and leading to the enhanced thermoelectric performance in a wide working temperature range, especially for the near/lower than room temperature range. This finding reveals that regulating the electron–electron correlation effects in solids has seen advances in the control of charge carrier concentrations, with promising signs for designing new thermoelectric materials.

Inspired by the strategy of controlling the carrier concentrations in the material system with phase transition behavior, other kinds of materials with their intrinsic phase transition also show promising signs for tailoring the optimal thermoelectric performance. For example, silver chalcogenides were the typical phase transition material system, having a fully-reversible phase transition between semiconductor and superior conductor.[165–167] Especially, at room temperature, Ag_2Se crystallizes in the orthorhombic phase, exhibiting a narrow-gap semiconducting behavior.[168] While at higher temperatures, α-Ag_2Se has a cubic crystal system, in which the silver atoms are statistically located in the interstitial sites among the Se bcc lattice. For this high-temperature phase, the Ag^+ cations move easily, exhibiting superionic conductivity.[169,170] Ag_2Se undergoes a fully-reversible first-order phase transition with a drastic electroresistivity change, tailoring for modulation of the electric properties to optimize the thermoelectric power factor. Indeed, based on the semiconductor-superionic conductor transition, the optimized power factor is obtained around the phase transition temperature for silver chalcogenides.[171] Regulating the phase transition behavior allows advances in balancing the electronic and thermal properties, showing promising signs for achieving the optimal thermoelectric performances in solids.[172]

5.2.2 Using metal–insulator domain walls in VO_2 to investigate the thermoelectric effect. Interfacing different materials is well-known as an effective way to enhance the thermoelectric effect from homogenous phase materials. For example, homogeneous doping in a single-crystalline material leads to a higher Seebeck coefficient;[173] InGaAs/InGaAlAs superlattices, embedded with randomly distributed ErAs nanoparticles, resulted in the enhancement of the Seebeck coefficient.[174] That is to say, that engineering the physical interfaces by forming junctions between the semiconductor/metal, or with bandgap offsets between two kinds of semiconductors would enhance the thermoelectric performance. In this regard, the VO_2 one-dimensional structures, such as the nano/microbeams, offer a material platform for investigating the thermoelectric effects with/without Schottky junctions. As is known, VO_2 undergoes a fully-reversible MIT at 68 °C with a structural phase transition from the high-temperature metallic rutile phase to low-temperature insulating monoclinic phase. When in the close vicinity of the phase transition temperature, multiple metal/insulator domain walls are aligned one-dimensionally along the nano/microbeams. Therefore, the metal/insulator Schottky junctions would form at the metal/insulator domain wall, and this process is fully reversible with the generation and elimination of the Schottky junctions. The vanadium dioxides then provide a fascinating material system to probe the junction-effect dependent thermoelectric performances.

The effect of domain wall on the Seebeck coefficient performance could be investigated by measuring the intrinsic thermal and electrical properties of a single VO_2 microbeam nanodevice.[175] For the microbeams clamped on the SiO_2 surface, under the intermediate environmental temperatures of 50–100 °C, the metallic and insulating phase were coexisting in one microbeam, forming the well-defined metal/insulating domain walls as the Schottky junctions (Fig. 20a). Below 50 °C, it is in the insulating phase; while above 100 °C, it is homogeneously in the metallic phase. In their case, the measurement of the Seebeck coefficient on the microbeams gives the values of −300 to −400 μV C^{-1} for the insulator phase, and −18 to −25 μV C^{-1}

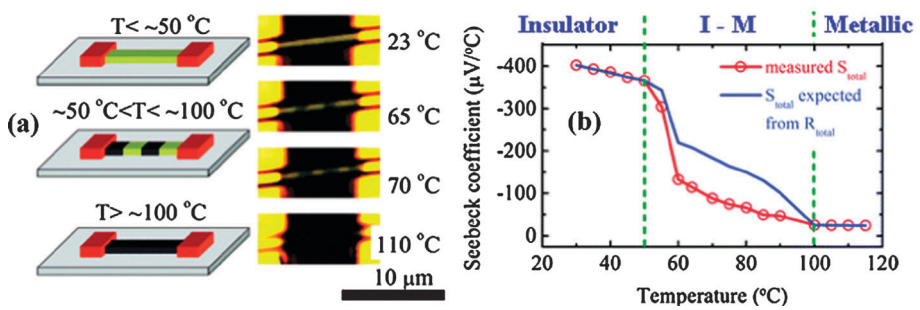

Fig. 20 Effect of the domain walls on the Seebeck effect in micro/nanobeams. (a) Optical microscopy images of a typical vanadium dioxide microbeam device taken at the environmental temperature of 23, 65, 70, and 110 °C, respectively, showing pure insulator and metal phases at lower and higher temperatures. The coexisting insulating and metallic domains could be clearly seen at the intermediate temperatures of 50–100 °C. (b) Temperature-dependent Seebeck coefficient of a VO_2 microbeam device. The solid red line is the experimentally measured Seebeck coefficient, and the solid blue line is the theoretically expected value. (Adapted with permission from ref. 175, Copyright 2011 American Chemical Society.)

for the metallic phase, respectively. For the phase coexisting regime, with the presence of multiple metal/insulator domain walls, the measured Seebeck effect is significantly lower than the expected value, by a factor of 2, as shown in Fig. 20b. The value discrepancy originates from the neglected domain wall contribution, that brought us complications with a nonlinear physical-phenomena effect. In this case, although the Seebeck effect of the vanadium dioxide microbeams across their metal–insulator domain walls has been investigated, they observed a negative effect on the Seebeck effect coming from the domain formed junctions. In effect, while the investigation of the Seebeck effect on the confined dimensional systems is in its early stages, how to effectively enhance the Seebeck effect by regulating the structural parameters in the single-domain nanostructures or surface modification of functional molecules are expected. Surely, in this case, to further dope heterogeneous ions in the single domain is another interesting topic, in which the structural derivation by the different kinds of involved metal ions provides multiple controllable parameters for regulating the potential thermoelectric effects in material systems with MITs. Since there is a rich material catalogue for materials having MIT behavior, systematic investigation on the effect of confined dimensionality of nano/microbeams on the thermoelectric effect, especially for the domain walls upon the phase transition process, shows promising signs for enhancing thermoelectric performances in the near future.

5.3 Fully-reversible metal–insulator transition for energy utilization applications

5.3.1 Fully-reversible metal–insulator transition for thermochromic smart windows by regulating the infrared-light. VO_2(M) possesses fully-reversible MITs triggered by changes in the environmental temperature, accompanied with a distinct change in its infrared transmittance.[18] As shown in Fig. 21a, the tetragonal lattice of VO_2(R) with the *P*42/*mnm* space group has a higher symmetry structure, bringing about a metallic behavior and infrared light blocking; while VO_2(M) with the *P*21/*c* space group (M1 phase) has a lower symmetry structure, providing a semiconducting behavior and infrared light transmission.[176,177] The large discrepancy of optical properties, especially in the infrared region (Fig. 21b), makes vanadium dioxide VO_2(M)–VO_2(R) an intriguing platform for smart windows, arising from the well-known thermochromic phenomena.[178] For the smart window application, the use of VO_2(M) films for energy-saving coatings for windows could then block out the incident infrared light, as a component of solar radiation, when the temperature is higher in the summer; while in the meantime allowing the infrared light incident to pass through when the temperature is decreased in cold weather. The whole process is fully reversible and thereby reduces the energy utility expense as a smart window.

The VO_2(M)–VO_2(R) system for smart windows still has some practical problems that restrict its use in industrial applications. To apply the VO_2 to a smart window, several issues must be addressed, including the low visible transmittance, weak optical contrast in the IR region, as well as the high MIT

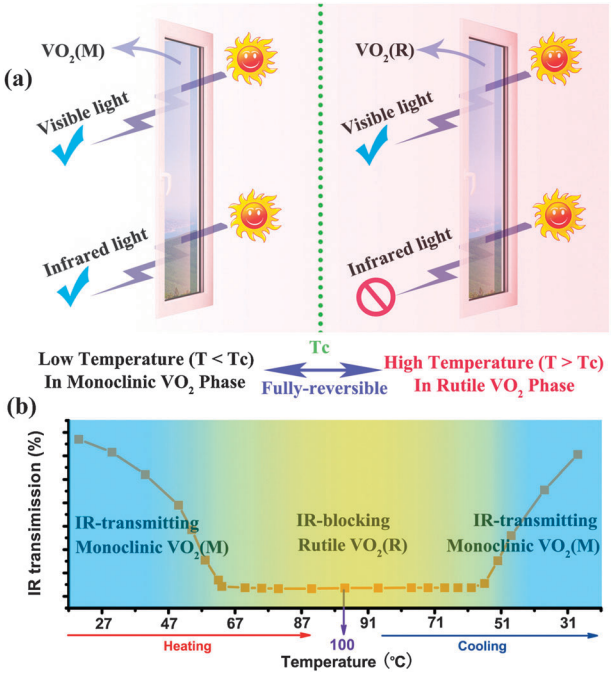

Fig. 21 (a) Schematic illustration of the mechanism of thermochromic smart windows based on the fully-reversible phase transition in VO_2(M/R). The higher temperature of the MIT temperature (T_c) leads to the formation of the rutile phase that could successfully block the transmission of infrared light, to mitigate the thermo-effect from the solar light energy. (b) Temperature dependence of the IR intensity at 2000 cm^{-1} (5000 nm) for a typical phase transition process by heating and cooling.

temperatures, *etc.*[179] For VO_2(M), the low visible transmittance originates from its intrinsic physical properties, where the strong innerband and interband absorptions for both the metallic and semiconductive states give the strong absorption of visible light in the short-wavelength range, exhibited by the black color of the sample.[180] The change in NIR transmittance before and after the MIT, known as the NIR switching efficiency (ΔT), is also a vital parameter for constructing smart windows.[181] Pure VO_2(M) usually exhibits excellent ΔT values, due to the quality of the sample.[182] The phase transition temperature of VO_2(M) is around 68 °C, which is considerably higher than room temperature. For the smart window, it usually requires the synergic advantages of high visible transmittance, obvious optical contrast in the IR region, as well as the right MIT temperature.

However, there is a strong correlation between these three parameters. For example, an increase in the film amount of VO_2(M) would increase the NIR switching efficiency (ΔT);[183] but in the meantime, the added mass also degrades the visible transmittance. Doping some donor impurity atoms, such as cations of Mo^{6+} and W^{6+} (having higher valence states) or anions of F^-, which provide the vanadium oxide system with extra electrons in the lattice frameworks and thus lowers the MIT temperature.[184] The doping of heterogeneous ions can result in a significant depression of the transition temperature, which then approaches room temperature; however, it is

usually at the expense of lowering the NIR switching efficiency (ΔT) with a weaker optical contrast in the IR region.[185–187] For example, by introducing ion defects and oxygen vacancies into the VO_2 system, the sample lowers the MIT temperature to 57.2 °C,[188] which accompanies a lower phase-transition performance of less enthalpy change and lower IR change ability.

A feasible way to reach a sufficient luminous transmittance is to involve other wide bandgap oxides in the VO_2(M) material system. A material with a wide bandgap would give a strong adsorption in the ultraviolet region, but a high transmission for the whole range of visible light, with the potential to enhance the luminous transmittance of the VO_2-including film.[189] In this regard, the TiO_2 and SiO_2 were the two most acceptable materials, having wide band gaps with high visible light transmission. The large-area VO_2–SiO_2 opals, with fine control over the filling volume by reducing vanadium pentoxide to vanadium dioxide, achieves drastic changes in the reflectance light that is promising for smart window applications.[190] Also, three-layer structures incorporating VO_2 and TiO_2, as well as VO_2 and SiO_x,[191,192] provide a partial solution to the visible transmission problem; while the five layers of $TiO_2/VO_2/TiO_2/VO_2/TiO_2$ offer more advantages, including angular performance.[193] Recent progress was also made by using SiO_2/VO_2 core/shell nanostructures, with which a transparent and flexible composite foil with excellent thermochromic properties for smart window applications could be successfully constructed.[194]

The development of designed nanostructured configurations also provides an effective way to modulate the trade-offs between the optical properties and MIT transition parameters. This is a technological pathway to harmonize these two parameters. Nanostructure configuration offers the transmission of visible light, and in the meantime, the excellent IR regulation ability would greatly promote the application of the fully-reversible VO_2 in practical applications. Fascinatingly, some successful progresses have been reported for promoting smart windows by using the designed VO_2 nanostructures. VO_2 films with different thicknesses and porosities at the nanoscale have successfully enhanced the performance to give more visible phonons to transmit.[195] The existence of a designed VO_2(M) nanoporous structure, whose size is out of the scattering range in the visible region, significantly enhanced the contributions to an increase of visible-light transmittance in the VO_2(M) thin film; while the interconnected crystalline VO_2(M) particles (forming a continuous particulate film) ensures the high NIR switching efficiency. In this regard, the thin film with a designed nanoporous structure resulted in high visible transmittance and a high NIR switching efficiency.[196]

VO_2 nanostructures, with different morphology configurations, provide a new promising pathway to gain the synergic advantages of lower MIT temperature, high luminous transmittance and excellent solar modulating ability. The VO_2 nanoparticle films prepared by the deposition of a precursor solution with PVP, and the film constructed by the nanoparticles gives excellent optical properties, bringing an integral visible transmittance of 54.5% and an optical contrast in the IR region of 41.5% at 2000 nm.[197] As shown in Fig. 22, the smaller nanosized

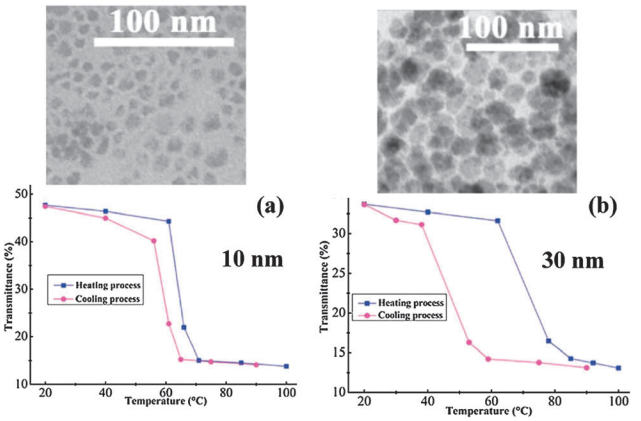

Fig. 22 The smaller nanosized VO_2 quantum dots showing the high luminous transmittance, excellent solar modulating ability as well as the narrower hysteresis width, showing more fascinating features for applications in thermochromic smart windows. The corresponding FT-IR transmittance *versus* environmental temperature curves for the 10 nm (a), and 30 nm (b) VO_2(M) nanocrystals. Inset are the high magnification TEM images of the VO_2 quantum dots with 10 nm and 30 nm sizes, respectively. (Adapted with permission from ref. 198, Copyright 2011 Royal Society of Chemistry.)

VO_2, down to 10 nm, indeed gives the synergic advantages of a narrowed hysteresis width, high transmittance, as well as the larger transmittance difference,[198] all of which were ideal for materials for smart windows. The high-quality 10 nm VO_2 nanocrystals, with higher specific surface areas, resulted in the increase of the number the defects, which have a stronger driving force to induce their phase transitions due to the presence of richer nucleation points.[199,200] As a result, the phase transition occurred at lower temperatures upon heating and at higher temperatures upon cooling, leading to the formation of remarkably narrowed hysteresis. Moreover, since it is well-known that the scattering efficiency gradually decreases with the reduction of particle size,[201] the transmittance of the 10 nm VO_2(M) nanocrystals obviously increases due to the smaller particle size. As a consequence, not only the optical transmittance, but also the transmittance difference before/after phase transition, greatly improved due to the decrease of the particle size down to 10 nm, as shown in Fig. 22. The synthetic single-domain VO_2(M) nanocrystals, with different diameter sizes, would provide an intriguing material platform for the construction of smart windows with the synergic advantages of high visible-light transmittance and excellent high NIR switching efficiency.

The fully-reversible MIT for thermochromic smart windows, based on a monoclinic/rutile VO_2 system, has important implications on the infrared light modulation for smart window applications, and on-going investigations are still much needed in the near future. Besides the above analyses, controlling the structural lattice arrangement provides opportunities for promoting the smart window performance of the monoclinic/rutile VO_2 system. For example, the MIT behavior is also found to be very sensitive to the oxygen stoichiometry and microstructures.[202] Also, the structural design of new crystal forms of vanadium oxides could be a potentially new way to mitigate the practical

problems when applying VO_2 to smart windows. Although several new crystallographic structures of vanadium oxides have been reported with the switching properties, they still seem far from practical application in smart windows. The problems at the present time are that all the samples are dark with a low visible-light transmission ability, as well as possessing an inappropriate MIT temperature.

5.3.2 Metal–insulator transition for magnetocaloric effects. Magnetic refrigeration (MR), based on the MCE, represents an environmentally-friendly and highly-efficient cooling technology for avoiding the impact of synthetic refrigerants on the environment as well as the legal safety obligations for the use of conventional gas compression refrigerators, with completely avoiding the damaging chemical gases [such as chlorofluorocarbons (CFCs) and hydrochlorofluorocarbons (HCFCs)] and reducing the CO_2 release.[203] Magnetocaloric refrigerators realize refrigeration based on the MCE, in which a low temperature can be attained when a magnetic field is applied isothermally and removed adiabatically.[204] The MCE highly depends on the entropy change of the magnetic moments, thus, the MCE can be observed in the vicinity of the first order paramagnetic–ferromagnetic transition,[205] from which a reorientation of the magnetic moment occurs when a magnetic field is applied. From this point of view, a giant MCE has been found in rare earth metal-based compounds, such as Gd–Si–Ge[206] and La–Ca–Sr–Mn–O systems.[207] Moreover, the order of the MCE is also dependent on the value of magnetization change with respect to temperature.[205] In this regard, 3d transition metal compounds, with magnetic ordering phase transitions, are another important material to realize the MCE. The MIT transition of VO_2(M)–VO_2(R) system also provides a material platform to display the MCE. In detail, the magnetization change in VO_2(M) at the first-order structural phase transition causes VO_2(M) to display a promising MCE. As is known, the position shifting of V^{4+} atoms from zigzag-type to linear chains answers for the MIT from VO_2(M) to VO_2(R), accompanying the evolution from the localized d-orbital electron cloud to the delocalized state along the c_R-axis direction. The orientation change of the electron cloud triggers the change of the state of electron spin and the magnetic moment on passing through the phase transition.[208] In fact, the change of magnetic moment during the MIT process constructs the bridge between the VO_2(M) and MCE.

To systematically understand the MCE in VO_2(M), our group used three samples to evaluate the MCE performance. That is, the single-domain nanorods from the solution-based synthetic sample, with other bulk samples that were prepared from conventional solid-state reactions and confined space combustion methods. Fig. 23a shows the $M(T)$ around the transition for the three VO_2(M) samples in a magnetic field of 200 Oe, where the ZFC curves clearly show the discontinuity at the transition. The change of magnetic susceptibility is due to the ordering change of the magnetic moment that originates from the positive Van Vleck paramagnetism and the negative diamagnetic susceptibility in the VO_2(M)–VO_2(R) system. The M–T curve for the VO_2(M) nanorods has the sharpest increasing trend at the transition temperature, and it is the rapid change of magnetization that would cause a large magnetic entropy change, bringing about the larger MCE. Fig. 23b shows the corresponding field dependence of the magnetization $M(H)$ for the VO_2(M) samples, in which curve 1, 2, and 3 denotes the solution synthetic sample, solid-state reaction sample and confined-space combustion sample, respectively. In this case, the VO_2(M) nanorods from the solution synthesis sample exhibits the largest step height before and after the structural phase transition, giving the performance advantage. The magnetic

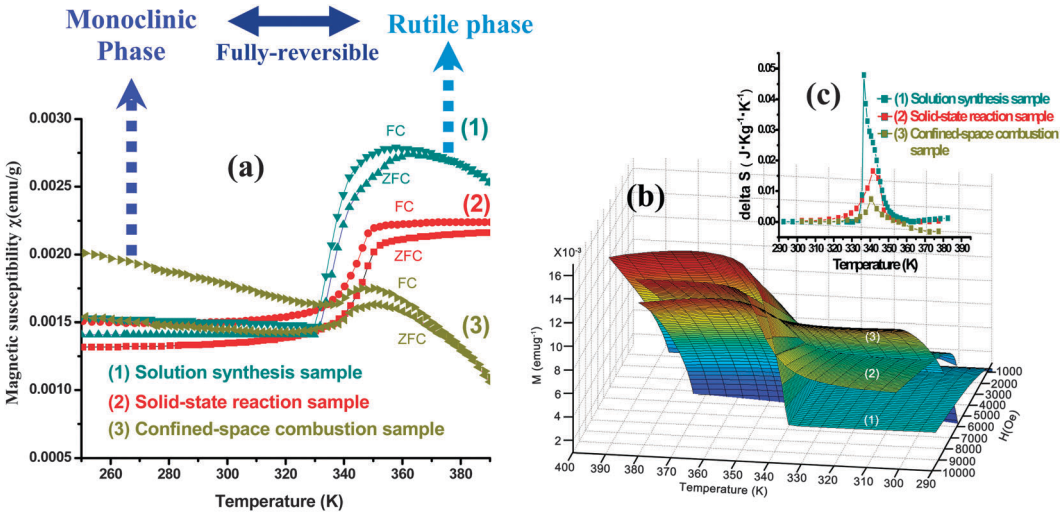

Fig. 23 Applying the fully-reversible MIT to the MCE. (a) Temperature dependence of ZFC and FC magnetization in an applied field of 200 Oe for VO_2(M) samples obtained from the solution synthesis (1), solid-state reaction (2), and confined-space combustion methods (3). (b) Magnetization isothermals in a heating temperature range of 290 K–390 K in different temperature steps for VO_2(M) samples from solution synthesis (Curve 1), solid state reactions (Curve 2), and confined-space combustion (Curve 3). (c) Magnetic entropy change ΔS of the VO_2(M) samples from solution synthesis (dark cyan curve), solid state reactions (red curve), and confined-space combustion (dark yellow curve). (Adapted with permission from ref. 103, Copyright 2011 Royal Society of Chemistry.)

entropy changes ΔS can be calculated from the field dependence of the magnetization $M(H)$ data by means of the Maxwell relation equation. As expected, the maximal value of ΔS_M for the VO_2(M) nanorod sample is 0.048 J Kg^{-1} K^{-1}, which is much larger than those of the other two bulk VO_2(M) samples for the solid-state reactions (0.017 J Kg^{-1} K^{-1}) and space-confined combustion methods (0.007 J Kg^{-1} K^{-1}) (Fig. 23c). The performance advantages for the single-domain VO_2(M) nanorods were due to the high-quality products with optimum atomic alignment, in which no obvious defects and structural distortions can be detected. In the VO_2 nanorods, the structural characteristics benefit the rapid magnetization change in the single-domain structure, leading to the better MCE. The large magnetic entropy change ΔS value near room temperature gives the first vanadium oxide compound displaying a MCE for magnetic refrigeration applications, which paves the way for the design of new MCE materials that are not limited to conventional systems, such as perovskites, complex alloys and rare earth magnets.[209–212] In a word, the fully-reversible MIT of VO_2(M) paves the way for further enhancing the MCE in future investigations.

6. Conclusions and outlook

In this review, we have outlined both the conventional strategies and recent progress made to bring correlated vanadium oxide systems to energy applications. The design of vanadium oxides with special microstructural characteristics has led to the regulation of electron–electron correlations with desired electronic structures, thereby opening the door for applying vanadium oxides in energy-related applications, such as energy storage (lithium ion batteries and supercapacitors), energy conversion (thermoelectrical devices), and energy utilization (''smart windows'' and magnetic refrigerators).

Although considerable progress has been made in engineering the electronic structure for correlated systems, owing to the structural design of vanadium oxides, there are still practical challenges and obstacles at the current stage. For materials with strong correlation effects, DFT calculations usually fail to precisely predict their electrical properties.[213] Moreover, the rich coordination styles and valence states in vanadium oxides significantly hamper the control of the crystal polymorphs in the pure phases, due to the tendency for oxidization or reduction under the synthetic conditions. For vanadium oxides, we have shown a series of new-phased materials and the synthetic mineral phases from the chemical synthetic methodologies; however, there is still room to pursue new vanadium materials with unique electrical properties, with which, the continual performance optimization of energy-related applications can be expected within the scope of available material chemistry and solid-state and energy science.

We also envision that the modulation of electron–electron correlations could be developed into a general route to control the physicochemical properties of functional materials, and thus it will find promising applications with a wider scope. For example, by regulating the e–e correlation in the engineering of electronic structures, it would give promising materials for applications in solar energy conversion and photovoltaics, in which the band gap is a determinative parameter for performance. By regulating the correlation effects in functional materials, bridges can be built between the atomic lattice, electronic structures and the practical energy-related applications, offering alternative promising solutions to promote future industrial processes to develop more diversified electrical properties of solid materials.

Acknowledgements

This work was financially supported by the National Basic Research Program of China (No. 2009CB939901), National Natural Science Foundation of China (No. 21222101, 11074229, 11132009, 11079004), Program for New Century Excellent Talents in University and Chinese Universities Scientific Fund (CUSF), and the Fundamental Research Funds for the Central Universities (No. WK2340000035 and WK2310000024).

References

1 N. S. Malvankar, M. Vargas, K. P. Nevin, A. E. Franks, C. Leang, B. C. Kim, K. Inoue, T. Mester, S. F. Covalla, J. P. Johnson, V. M. Rotello, M. T. Tuominen and D. R. Lovley, *Nat. Nanotechnol.*, 2011, **6**, 573.
2 H. W. Jang, D. A. Felker, C. W. Bark, Y. Wang, M. K. Niranjan, C. T. Nelson, Y. Zhang, D. Su, C. M. Folkman, S. H. Baek, S. Lee, K. Janicka, Y. Zhu, X. Q. Pan, D. D. Fong, E. Y. Tsymbal, M. S. Rzchowski and C. B. Eom, *Science*, 2011, **331**, 886.
3 P. L. Taberna, S. Mitra, P. Poizot, P. Simon and J.-M. Tarascon, *Nat. Mater.*, 2006, **5**, 567.
4 P. C. Canfield, *Nat. Mater.*, 2011, **10**, 259.
5 H. Ohno, *Science*, 1998, **281**, 951.
6 C. Z. Wu, H. O. Zhu, J. Dai, W. S. Yan, J. L. Yang, Y. C. Tian, S. Q. Wei and Y. Xie, *Adv. Funct. Mater.*, 2010, **20**, 3666.
7 T. Tokura, *Phys. Today*, 2003, **56**, 50.
8 J. Kim, C. Y. Wong and G. D. Scholes, *Acc. Chem. Res.*, 2009, **42**, 1037.
9 G. Pernot, M. Stoffel, I. Savic, F. Pezzoli, P. Chen, G. Savelli, A. Jacquot, J. Schumann, U. Denker, I. Mönch, Ch. Deneke, O. G. Schmidt, J. M. Rampnoux, S. Wang, M. Plissonnier, A. Rastelli, S. Dilhaire and N. Mingo, *Nat. Mater.*, 2010, **9**, 491.
10 D. Q. Chen, P. Huang, Y. L. Yu, F. Huang, A. P. Yang and Y. S. Wang, *Chem. Commun.*, 2011, **47**, 5801.
11 J. Wei, H. Ji, W. H. Guo, A. H. Nevidomskyy and D. Natelson, *Nat. Nanotechnol.*, 2012, **7**, 357.
12 C. Z. Wu, H. Wei, B. Ning and Y. Xie, *Adv. Mater.*, 2010, **22**, 1972.
13 F. J. Morin, *Phys. Rev. Lett.*, 1959, **3**, 34.
14 M. Nakano, K. Shibuya, D. Okuyama, T. Hatano, S. Ono, M. Kawasaki, Y. Iwasa and Y. Tokura, *Nature*, 2012, **487**, 459.

15 S. Biermann, A. Poteryaev, A. I. Lichtenstein and A. Georges, *Phys. Rev. Lett.*, 2005, **94**, 026404.
16 J. Cao, E. Ertekin, V. Srinivasan, W. Fan, S. Huang, H. Zheng, J. W. L. Yim, D. R. Khanal, D. F. Ogletree, J. C. Grossman and J. Wu, *Nat. Nanotechnol.*, 2009, **4**, 732.
17 J. B. Goodenough, *Annu. Rev. Mater. Sci.*, 1971, **1**, 101.
18 M. K. Liu, H. Y. Hwang, H. Tao, A. C. Strikwerda, K. B. Fan, G. R. Keiser, A. J. Sternbach, K. G. West, S. Kittiwatanakul, J. W. Lu, S. A. Wolf, F. G. Omenetto, X. Zhang, K. A. Nelson and R. D. Averitt, *Nature*, 2012, DOI: 10.1038/nature11231.
19 M. G. Park, X. C. Zhang, M. Chung, G. B. Less and A. M. Sastry, *J. Power Sources*, 2010, **795**, 1904.
20 S. Y. Chung, J. T. Bloking and Y. M. Chiang, *Nat. Mater.*, 2002, **1**, 123.
21 K. S. Park, A. Benayad, D. J. Kang and S. G. Doo, *J. Am. Chem. Soc.*, 2008, **130**, 14930.
22 G. Yu, L. Hu, N. Liu, H. Wang, M. Vosgueritchian, Y. Yang, Y. Cui and Z. Bao, *Nano Lett.*, 2011, **11**, 4438.
23 G. Yu, L. Hu, M. Vosgueritchian, H. Wang, X. Xie, J. R. McDonough, X. Cui, Y. Cui and Z. Bao, *Nano Lett.*, 2011, **11**, 2905.
24 H. L. Liu, X. Shi, F. F. Xu, L. L. Zhang, W. Q. Zhang, L. D. Chen, Q. Li, C. Uher, T. Day and G. J. Snyder, *Nat. Mater.*, 2012, **11**, 422.
25 Y. Z. Pei, X. Y. Shi, A. LaLonde, H. Wang, L. D. Chen and G. J. Snyder, *Nature*, 2011, **473**, 66.
26 F. J. Morin, *Phys. Rev. Lett.*, 1959, **3**, 34.
27 L. kritikos, L. Zanbelis, G. Papadinimitropoulos and D. Davazoglou, *Mater. Sci. Eng.*, 2007, **201**, 9334.
28 N. N. Greenwood and A. Earnshaw, *Chemistry of the elements*, Butterworth-Heinemann, UK, 2nd edn, 1997.
29 K. Kosuge, T. Takada and S. Kachi, *J. Phys. Soc. Jpn.*, 1963, **18**, 318.
30 A. Heidemann, K. Kosuge, Y. Ueda and S. Kachi, *Phys. Status Solidi A*, 1977, **39**, K37.
31 U. Schwingenschlogl and V. Eyert, *Ann. Phys.*, 2004, **13**, 475.
32 A. F. Wells, *Structural inorganic chemistry*, Oxford, Clarendon Press, 5th edn, 1984.
33 W. T. Liu, J. Cao, W. Fan, H. Zhao, C. M. Martin, Y. R. Shen, J. Wu and F. Wang, *Nano Lett.*, 2011, **11**, 466–470.
34 B. Hu, Y. Zhang, W. Chen, C. Xu and Z. L. Wang, *Adv. Mater.*, 2011, **23**, 3536–3541.
35 K. Appavoo and R. F. Haglund, *Nano Lett.*, 2011, **11**, 1025.
36 C. R. Everhart and J. B. MacChesney, *J. Appl. Lett.*, 1968, **39**, 2872.
37 D. B. McWhan, M. Marezio, J. P. Remeika and P. D. Dernier, *Phys. Rev. B: Condens. Matter Mater. Phys.*, 1974, **10**, 490.
38 E. Strelcov, Y. Lilach and A. Kolmakov, *Nano Lett.*, 2009, **9**, 2322.
39 R. Long, B. Y. Qu, R. C. Tan, Y. F. Sun, X. G. Tan, W. Ying, B. C. Pan, Y. J. Xiong and Y. Xie, *Phys. Chem. Chem. Phys.*, 2012, **14**, 7225.
40 Z. Chen, Y. F. Gao, L. T. Kang, J. Dua, Z. T. Zhang, H. J. Luo, H. Y. Miao and G. Q. Tan, *Sol. Energy Mater. Sol. Cells*, 2011, **95**, 712.
41 M. Imada, A. Fujimori and Y. Tokura, *Rev. Mod. Phys.*, 1998, **70**, 1039.
42 R. M. Wentzcovitch, W. W. Schulz and P. B. Allen, *Phys. Rev. Lett.*, 1994, **72**, 3389.
43 T. M. Rice, H. Launois and J. P. Pouget, *Phys. Rev. Lett.*, 1994, **73**, 3042.
44 M. Gatti, F. Bruneval, V. Olevano and L. Reining, *Phys. Rev. Lett.*, 2007, **99**, 266402.
45 M. M. Qazilbash, M. Brehm, B. G. Chae, P. C. Ho, G. O. Andreev, B.-J. Kim, S. Jin Yun, A. V. Balatsky, M. B. Maple, F. Keilmann, H.-T. Kim and D. N. Basov, *Science*, 2007, **318**, 1750.
46 P. B. Allen, R. M. Wentzcovitch, W. W. Schulz and P. C. Canfield, *Phys. Rev. B: Condens. Matter Mater. Phys.*, 1993, **48**, 4359.
47 V. J. Emery and S. A. Kivelson, *Phys. Rev. Lett.*, 1995, **74**, 3253.
48 J. Wu, Q. Gu, B. S. Guiton, N. P. de Leon, L. Ouyang and H. Park, *Nano Lett.*, 2006, **6**, 2313–2317.
49 J. Wei, Z. H. Wang, W. Chen and D. H. Cobden, *Nat. Nanotechnol.*, 2009, **4**, 420.
50 V. Eyert, *Ann. Phys.*, 2002, **11**, 650.
51 J. B. Cao and J. Q. Wu, *Mater. Sci. Eng., R*, 2011, **71**, 35.
52 B. Hu, Y. Ding, W. Chen, D. Kulkarni, Y. Shen, V. V. Tsukruk and Z. L. Wang, *Adv. Mater.*, 2010, **22**, 5834.
53 Y. Tokura, *J. Phys. Soc. Jpn.*, 2006, **75**, 011001.
54 A. Pashkin, C. Kübler, H. Ehrke1, R. Lopez, A. Halabica, R. F. Haglund, R. Huber and A. Leitenstorfer, *Phys. Rev. B: Condens. Matter Mater. Phys.*, 2011, **83**, 195120.
55 A. Cavalleri, C. Toth, C. W. Siders, J. A. Squier, F. Raksi, P. Forget and J. C. Kieffer, *Phys. Rev. Lett.*, 2001, **87**, 237401.
56 P. Baum, D. S. Yang and A. H. Zewail, *Science*, 2007, **318**, 788.
57 M. S. Grinolds, V. A. Lobastov, J. Weissenrieder and A. H. Zewail, *Proc. Natl. Acad. Sci. U. S. A.*, 2006, **103**, 18427.
58 T. Yao, X. Zhang, Z. Sun, S. Liu, Y. Huang, Y. Xie, C. Wu, X. Yuan, W. Zhang, Z. Wu, G. Pan, F. Hu, L. Wu, Q. Liu and S. Wei, *Phys. Rev. Lett.*, 2010, **105**, 226405.
59 X. G. Tan, T. Yao, R. Long, Z. H. Sun, Y. J. Feng, H. Cheng, X. Yuan, W. Q. Zhang, Q. H. Liu, C. Z. Wu, Y. Xie and S. Q. Wei, *Sci. Rep.*, 2012, **2**, 466.
60 C. H. Griffiths and H. K. Eastwood, *J. Appl. Phys.*, 1974, **45**, 2201.
61 P. F. Bongers, *Solid State Commun.*, 1965, **3**, 275.
62 L. Whittaker, C. Jaye, Z. G. Fu, D. A. Fischer and S. Banerjee, *J. Am. Chem. Soc.*, 2009, **131**, 8884.
63 C. Z. Wu, W. Xie, M. Zhang, L. F. Bai, J. L. Yang and Y. Xie, *Chem.–Eur. J.*, 2009, **15**, 492.
64 Y. L. Li and T. Ishigaki, *J. Cryst. Growth*, 2002, **242**, 511.
65 C. Z. Wu, F. Feng, J. Feng, J. Dai, J. L. Yang and Y. Xie, *J. Phys. Chem. C*, 2011, **115**, 791.
66 C. Z. Wu, L. Y. Lei, X. Zhu, J. L. Yang and Y. Xie, *Small*, 2007, **3**, 1518.
67 L. T. Kang, Y. F. Gao and H. J. Luo, *ACS Appl. Mater. Interfaces*, 2009, **1**, 2211.
68 T. D. Manning, I. P. Parkin, M. E. Pemble, D. Sheel and D. Vernardou, *Chem. Mater.*, 2004, **16**, 744.

69 S. Loffler, E. Auer, M. Weil, A. Lugstein and E. Bertagnolli, *Appl. Phys. A*, 2011, **102**, 201.
70 C. Z. Wu, L. Y. Lei, X. Zhu, J. L. Yang and Y. Xie, *Small*, 2007, **3**, 1518.
71 T. D. Manning, I. P. Parkin, M. E. Pemble, D. Sheel and D. Vernardou, *Chem. Mater.*, 2004, **16**, 744.
72 B. S. Guiton, Q. Gu, A. L. Prieto, M. S. Gudiksen and H. K. Park, *J. Am. Chem. Soc.*, 2005, **127**, 498.
73 C. Z. Wu, J. Dai, X. D. Zhang, J. L. Yang, F. Qi, C. Gao and Y. Xie, *Angew. Chem., Int. Ed.*, 2010, **49**, 134.
74 J. F. Xie, C. Z. Wu, S. L. Hu, J. Dai, N. Zhang, J. Feng, J. L. Yang and Y. Xie, *Phys. Chem. Chem. Phys.*, 2012, **14**, 4810.
75 S. Turner and P. R. Buseck, *Nature*, 1983, **304**, 143.
76 H. T. Evans and M. E. Mrose, *Am. Mineral.*, 1950, **40**, 861.
77 Z. Gui, R. Gan, W. Mo, X. Chen, L. Yang, S. Zhang, Y. Hu, Z. Wang and W. Fan, *Chem. Mater.*, 2002, **14**, 5053.
78 B. S. Guiton, Q. Gu, A. L. Prieto, M. S. Gudiksen and H. K. Park, *J. Am. Chem. Soc.*, 2005, **127**, 498.
79 Z. R. Dai, Z. W. Pan and Z. L. Wang, *Adv. Funct. Mater.*, 2003, **13**, 9–24.
80 R. G. Xie, C. T. Bui, B. Varghese, Q. X. Zhang, C. H. Sow, B. W. Li and J. T. L. Thong, *Adv. Funct. Mater.*, 2011, **21**, 1602.
81 Y. Cheng, T. L. Wong, K. M. Ho and N. Wang, *J. Cryst. Growth*, 2009, **311**, 1571.
82 M. H. Kim, B. D. Lee, S. Lee, C. Larson, J. M. Baik, O. C. T. Yavuz, S. Seifert, S. Vajda, R. E. Winans, M. Moskovits, G. D. Stucky and A. M. Wodtke, *Nano Lett.*, 2009, **9**, 4138.
83 A. Y. Borisevich and P. K. Davies, *J. Am. Ceram. Soc.*, 2004, **87**, 1047.
84 J. I. Sohn, H. J. Joo, A. E. Porter, C. J. Choi, K. Kim, D. J. Kang and M. E. Welland, *Nano Lett.*, 2007, **7**, 1570.
85 Y. J. Cui, X. W. Wang, Y. Zhou, R. Gordon and S. Ramanathan, *J. Cryst. Growth*, 2012, **338**, 96.
86 J. F. De Natale, P. J. Hood and A. B. Harker, *J. Appl. Phys.*, 1989, **66**, 5844.
87 A. Haras, M. Witko, D. R. Salahub, K. Hermann and R. Tokarz, *Surf. Sci.*, 2001, **491**, 77.
88 B. Hu, Y. Ding, W. Chen, D. Kulkarni, Y. Shen, V. V. Tsukruk and Z. L. Wang, *Adv. Mater.*, 2010, **22**, 5134.
89 C. Cheng, K. Liu, B. Xiang, J. Suh and J. Q. Wu, *Appl. Phys. Lett.*, 2012, **100**, 103111.
90 J. H. Son, J. Wei, D. Cobden, G. Z. Cao and Y. N. Xia, *Chem. Mater.*, 2010, **22**, 3043.
91 S. D. Zhang, Y. M. Li, C. Z. Wu, F. Zheng and Y. Xie, *J. Phys. Chem. C*, 2009, **113**, 15058.
92 J. F. Liu, Q. H. Li, T. H. Wang, D. P. Yu and Y. D. Li, *Angew. Chem., Int. Ed.*, 2004, **43**, 5048.
93 L. Whittaker, C. Jaye, Z. Fu, D. Fischer and S. Banerjee, *J. Am. Chem. Soc.*, 2009, **131**, 8884.
94 E. J. Felten, D. E. Fornwalt and A. V. Karg, *J. Solid State Chem.*, 1970, **2**, 295.
95 C. X. Cao, Y. F. Gao and H. J. Luo, *J. Phys. Chem. C*, 2008, **112**, 18810.
96 D. T. Cromer and K. Herrington, *J. Am. Chem. Soc.*, 1955, **77**, 4708.
97 T. Kubo, H. Orita and H. Nozoye, *J. Am. Chem. Soc.*, 2007, **129**, 10474.
98 J. K. Burdett, T. Hughbanks, G. J. Miller, J. W. Richardson and J. V. Smith, *J. Am. Chem. Soc.*, 1987, **109**, 3639.
99 J. P. Jolivet, *Metal oxide chemistry and synthesis: from solution to solid state*, Wiley, West Sussex, 2003.
100 H. Y. Zhu, Y. Lan, X. P. Gao, S. P. Ringer, Z. F. Zheng, D. Y. Song and J. C. Zhao, *J. Am. Chem. Soc.*, 2005, **127**, 6730.
101 R. C. Bell, K. A. Zemski and A. W. Castleman, *J. Cluster Sci.*, 1999, **10**, 509.
102 T. Chirayil, P. Y. Zavalij and M. Stanley Whittingham, *Chem. Mater.*, 1998, **10**, 2629.
103 C. Z. Wu, X. D. Zhang, J. Dai, J. L. Yang, Z. Y. Wu, S. Q. Wei and Y. Xie, *J. Mater. Chem.*, 2011, **21**, 4509.
104 J. H. Son, J. Wei, D. Cobden, G. Z. Cao and Y. N. Xia, *Chem. Mater.*, 2010, **22**, 3043.
105 A. M. Cao, J. S. Hu, H. P. Liang and L. J. Wan, *Angew. Chem., Int. Ed.*, 2005, **44**, 4391.
106 H. J. Muhr, F. Krumeich, U. P. Schönholzer, F. Bieri, M. Niederberger, L. J. Gauckler and R. Nesper, *Adv. Mater.*, 2000, **12**, 231.
107 N. Pinna, U. Wild, J. Urban and R. Schlögl, *Adv. Mater.*, 2003, **15**, 329.
108 J. Liu, H. Xia, D. F. Xue and L. Lu, *J. Am. Chem. Soc.*, 2009, **131**, 12086.
109 X. F. Zhang, K. X. Wang, X. Wei and J. S. Chen, *Chem. Mater.*, 2011, **23**, 5290.
110 M. Wei, H. Sugihara, I. Honma, M. Ichihara and H. Zhou, *Adv. Mater.*, 2005, **17**, 2964.
111 H. T. Evans, Jr and S. Block, *Am. Mineral.*, 1953, **38**, 1242.
112 J. Chenavas, *J. Solid State Chem.*, 1973, **6**, 1.
113 J. Muller and J. C. Joubert, *J. Solid State Chem.*, 1974, **11**, 79.
114 H. T. Evans Jr and M. E. Mrose, *Am. Mineral.*, 1960, **45**, 1144.
115 L. LÖffler and W. Mader, *J. Am. Ceram. Soc.*, 2003, **86**, 534.
116 C. Z. Wu, Z. P. Hu, W. Wang, M. Zhang, J. L. Yang and Y. Xie, *Chem. Commun.*, 2008, 3891.
117 C. Z. Wu, J. Dai, X. D. Zhang, J. L. Yang and Y. Xie, *J. Am. Chem. Soc.*, 2009, **131**, 7218.
118 C. Z. Wu, S. Q. Hu, L. Y. Lei, P. Yin, T. W. Li and Y. Xie, *Microporous Mesoporous Mater.*, 2006, **89**, 300.
119 J. Goldberger, R. R. He, Y. F. Zhang, S. K. Lee, H. Q. Yan, H. J. Choi and P. D. Yang, *Nature*, 2003, **422**, 599.
120 N. Leventis, A. Sadekar, N. Chandrasekaran and C. Sotiriou-Leventis, *Chem. Mater.*, 2010, **22**, 2790.
121 Q. M. Shen, X. M. Zhao, S. W. Zhou, W. H. Hou and J. J. Zhu, *J. Phys. Chem. C*, 2011, **115**, 17958.
122 M. T. Ng, C. B. Boothroyd and J. J. Vittal, *J. Am. Chem. Soc.*, 2006, **128**, 7118.
123 K. M. Nam, Y. I. Kim, Y. H. J. S. M. Lee, B. G. Kim, R. Choi, S. I. Choi, H. J. Song and J. T. Park, *J. Am. Chem. Soc.*, 2012, **134**, 8392.
124 M. J. Redman and E. G. Steward, *Nature*, 1962, **193**, 867.
125 P. F. Lang and B. C. Smith, *Dalton Trans.*, 2010, **39**, 7786.
126 C. Z. Wu, Y. Xie, L. Y. Lei, S. Q. Hu and C. Z. OuYang, *Adv. Mater.*, 2006, **18**, 1727.

127 L. N. Moyes, R. H. Parkman, J. M. Charnock, D. J. Vaughan, F. R. Livens, C. R. Hughes and A. Braithwaite, *Environ. Sci. Technol.*, 2000, **34**, 1062.
128 C. Z. Wu, X. D. Zhang, B. Ning, J. L. Yang and Y. Xie, *Inorg. Chem.*, 2009, **48**, 6044.
129 L. Y. Li and D. L. King, *Chem. Mater.*, 2005, **17**, 4335.
130 A. L. J. Pereira, L. Gracia, A. Beltrán, P. N. Lisboa-Filho, J. H. D. da Silva and J. Andrés, *J. Phys. Chem. C*, 2012, **116**, 8753.
131 C. Z. Wu, H. Wei, B. Ning, J. L. Yang and Y. Xie, *Chem. Commun.*, 2010, **46**, 1845.
132 K. Held, G. Keller, V. Eyert, D. Vollhardt and V. I. Anisimov, *Phys. Rev. Lett.*, 2001, **86**, 5345.
133 D. J. M. Bevan and R. L. Martin, *J. Solid State Chem.*, 2008, **181**, 2250.
134 A. Vegas, R. L. Martin and D. J. M. Bevan, *Acta Crystallogr., Sect. B: Struct. Sci.*, 2009, **65**, 11.
135 Y. Xu, L. Zheng, C. Z. Wu, F. Qi and Y. Xie, *Chem.–Eur. J.*, 2011, **17**, 384.
136 V. V. Terskikh, I. L. Moudrakovski, C. I. Ratcliffe and J. A. Ripmeester, *J. Am. Chem. Soc.*, 2001, **123**, 2891.
137 D. Weber, A. Stork, S. Nakhal, C. Wessel, C. Reimann, W. Hermes, A. Muller, T. Ressler, R. Pottgen, T. Bredow, R. Dronskowski and M. Lerch, *Inorg. Chem.*, 2011, **50**, 6762.
138 C. Wessel, C. Reimann, A. Müller, D. Weber, M. Lerch, T. Ressler, T. Bredow and R. Dronskowski, *J. Comput. Chem.*, 2012, **33**, 2102.
139 E. M. Page and S. A. Wass, in *Encyclopedia of inorganic chemistry*, John Wiley & Sons, 1994.
140 R. M. Cornell and U. Schwertmann, *The iron oxides: structure, properties, reactions, occurrences and uses*, Wiley, VCH, 2003.
141 P. G. Bruce, S. A. Freunberger, L. J. Hardwick and J. M. Tarascon, *Nat. Mater.*, 2012, **11**, 19.
142 C. Xiao, J. Xu, K. Li, J. Feng, J. L. Yang and Y. Xie, *J. Am. Chem. Soc.*, 2012, **134**, 4287.
143 W. Li, J. R. Dahn and D. Wainwright, *Science*, 1994, **264**, 1115.
144 J. Y. Luo, W. J. Cui, P. He and Y. Y. Xia, *Nat. Chem.*, 2010, **2**, 760.
145 C. Z. Wu and Y. Xie, *Energy Environ. Sci.*, 2010, **3**, 1191.
146 Y. Xie and C. Z. Wu, *Dalton Trans.*, 2007, 5235.
147 B. G. Hyde, A. N. Bagshaw, S. Anderson and M. O. Keeffe, *Annu. Rev. Mater. Sci.*, 1974, **4**, 43.
148 C. Z. Wu, Z. P. Hu, W. Wang, M. Zhang, J. L. Yang and Y. Xie, *Chem. Commun.*, 2008, 3891.
149 K. Held, G. Keller, V. Eyert, D. Vollhardt and V. I. Anisimov, *Phys. Rev. Lett.*, 2001, **86**, 5345.
150 Y. F. Sun, S. S. Jiang, W. T. Bi, C. Z. Wu and Y. Xie, *J. Power Sources*, 2011, **196**, 8644.
151 J. Feng, L. L. Peng, C. Z. Wu, X. Sun, S. L. Hu, C. W. Lin, J. Dai, J. L. Yang and Y. Xie, *Adv. Mater.*, 2012, **24**, 1917.
152 Y. D. Ma, Y. Dai, M. Guo, C. W. Niu, Y. T. Zhu and B. B. Huang, *ACS Nano*, 2012, **6**, 1695.
153 J. N. Coleman1, M. Lotya, A. O'Neill, S. D. Bergin, P. J. King, U. Khan, K. Young, A. Gaucher, S. De, R. J. Smith, I. V. Shvets, S. K. Arora, G. Stanton, H. Y. Kim, K. H. Lee, G. T. Kim, G. S. Duesberg, T. Hallam, J. J. Boland, J. J. Wang, J. F. Donegan, J. C. Grunlan, G. Moriarty, A. Shmeliov, R. J. Nicholls, J. M. Perkins, E. M. Grieveson, K. Theuwissen, D. W. McComb, P. D. Nellist and V. Nicolosi, *Science*, 2011, **331**, 568.
154 Y. Zhu, S. Murali, M. D. Stoller, K. J. Ganesh, W. Cai, P. J. Ferreira, A. Pirkle, R. M. Wallace, K. Cychosz, M. Thommes, D. Su, E. A. Stach and R. S. Ruoff, *Science*, 2011, **332**, 1537.
155 J. Chmiola, C. Largeot, P. L. Taberna, P. Simon and Y. Gogotsi, *Science*, 2010, **328**, 480.
156 J. R. Miller, R. A. Outlaw and B. C. Holloway, *Science*, 2010, **329**, 1637.
157 S. Bae, H. Kim, Y. Lee, X. Xu, J. S. Park, Y. Zheng, J. Balakrishnan, T. Lei, H. Ri Kim, Y. I. Song, Y. J. Kim, K. S. Kim, B. Ozyilmaz, J. H. Ahn, B. H. Hong and S. Iijima, *Nat. Nanotechnol.*, 2010, **5**, 574.
158 J. Feng, X. Sun, C. Z. Wu, L. L. Peng, C. W. Lin, S. L. Hu, J. L. Yang and Y. Xie, *J. Am. Chem. Soc.*, 2011, **133**, 17832.
159 J. F. Li, W. S. Liu, L. D. Zhao and M. Zhou, *NPG Asia Mater.*, 2010, **2**, 152.
160 A. I. Hochbaum, R. K. Chen, R. D. Delgado, W. J. Liang, E. C. Garnett, M. Najarian, A. Majumdar and P. D. Yang, *Nature*, 2008, **451**, 163.
161 G. J. Snyder and E. S. Toberer, *Nat. Mater.*, 2008, **7**, 105.
162 C. Z. Wu, H. O. Zhu, J. Dai, W. S. Yan, J. L. Yang, Y. C. Tian, S. Q. Wei and Y. Xie, *Adv. Funct. Mater.*, 2010, **20**, 3666.
163 M. Nakano, K. Shibuya, D. Okuyama, T. Hatano, S. Ono, M. Kawasaki, Y. Iwasa and Y. Tokura, *Nature*, 2012, **487**, 459.
164 C. Z. Wu, F. Feng, J. Feng, J. Dai, L. L. Peng, J. Y. Zhao, J. L. Yang, C. Si, Z. Y. Wu and Y. Xie, *J. Am. Chem. Soc.*, 2011, **133**, 13798.
165 P. Helv, *J. Phys. Acta*, 1959, **32**, 567.
166 M. Kobayashi, *Solid State Ionics*, 1990, **39**, 121.
167 M. C. Santhosh Kumar and B. Pradeep, *Semicond. Sci. Technol.*, 2002, **17**, 261.
168 J. P. Ge, S. Xu, L. P. Liu and Y. D. Li, *Chem.–Eur. J.*, 2006, **12**, 3672.
169 P. Boolchand and W. J. Bresser, *Nature*, 2001, **410**, 1070.
170 M. Oliveria, R. K. McMullan and B. J. Wuensch, *Solid State Ionics*, 1988, **28–30**, 1332.
171 C. Xiao, J. Xu, K. Li, J. Feng, J. L. Yang and Y. Xie, *J. Am. Chem. Soc.*, 2012, **134**, 4287.
172 C. Xiao, J. Xu, B. X. Cao, K. Li, M. G. Kong and Y. Xie, *J. Am. Chem. Soc.*, 2012, **134**, 7971.
173 J. P. Heremans, V. Jovovic, E. S. Toberer, A. Saramat, K. Kurosaki, A. Charoenphakdee, S. Yamanaka and G. J. Snyder, *Science*, 2008, **321**, 554.
174 G. Zeng, J. M. O. Zide, W. Kim, J. E. Bowers, A. C. Gossard, Z. Bian, Y. Zhang, A. Shakouri, S. L. Singer and A. Majumdar, *J. Appl. Phys.*, 2007, **101**, 034502.
175 J. Cao, W. Fan, H. Zheng and J. Wu, *Nano Lett.*, 2009, **9**, 4001.
176 M. M. Qazilbash, A. A. Schafgans, K. S. Burch, S. J. Yun, B. G. Chae, B. J. Kim, H. T. Kim and D. N. Basov, *Phys. Rev. B: Condens. Matter Mater. Phys.*, 2008, **77**, 115121.

177 A. S. Barker, H. W. Verleur and H. J. Guggenheim, *Phys. Rev. Lett.*, 1966, **17**, 1286.
178 K. R. Speck, H. S. W. Hu, M. E. Sherwin and R. S. Potember, *Thin Solid Films*, 1988, **165**, 317.
179 N. R. Mlyuka, G. A. Niklasson and C. G. Granqvist, *Phys. Status Solidi A*, 2009, **206**, 2155.
180 M. M. Qazilbash, A. A. Schafgans, K. S. Burch, S. J. Yun, S. J. B. G. Chae, B. J. Kim, H. T. Kim and D. N. Basov, *Phys. Rev. B: Condens. Matter Mater. Phys.*, 2008, **77**, 115121.
181 G. Xu, P. Jin, M. Tazawa and K. Yoshimura, *Jpn. J. Appl. Phys.*, 2004, **43**, 186.
182 F. Béteille and J. Livage, *Chem. Mater. Sci.*, 1998, **13**, 915.
183 F. Guinneton, L. Sauques, J. C. Valmalette, F. Cros and J. R. Gavarri, *Thin Solid Films*, 2004, **446**, 287.
184 L. Whittaker, T. L. Wu, C. J. Patridge, G. Sambandamurthy and S. Banerjee, *J. Mater. Chem.*, 2011, **21**, 5580.
185 K. Shibuya, M. Kawasaki and Y. Tokura, *Appl. Phys. Lett.*, 2010, **96**, 022102.
186 M. Aryanpour, R. Hoffmann and F. J. DiSalvo, *Chem. Mater.*, 2009, **21**, 1627.
187 T. D. Manning, I. P. Parkin, M. E. Pemble, D. Sheel and D. Vernardou, *Chem. Mater.*, 2004, **16**, 744.
188 C. Z. Wu, F. Feng, J. Feng, J. Dai, J. L. Yang and Y. Xie, *J. Phys. Chem. C*, 2011, **115**, 791.
189 C. G. Granqvist, *Sol. Energy Mater. Sol. Cells*, 2007, **91**, 1529.
190 M. Ibisate1, D. Golmayo and C. Lopez, *J. Opt. A: Pure Appl. Opt.*, 2008, **10**, 125202.
191 P. Jin, G. Xu, M. Tazawa and K. Yoshimura, *Appl. Phys. A*, 2003, **77**, 455.
192 H. Kakiuchida, P. Jin and M. Tazawa, *Sol. Energy Mater. Sol. Cells*, 2008, **92**, 1279.
193 N. R. Mlyuka, G. A. Niklasson and C. G. Granqvist, *Phys. Status Solidi A*, 2009, **206**, 2155.
194 Y. F. Gao, S. B. Wang, H. J. Luo, L. Dai, C. X. Cao, Y. L. Liu, Z. Chen and M. Kanehira, *Energy Environ. Sci.*, 2012, **5**, 6104.
195 L. Whittaker, T. L. Wu, C. J. Patridge, G. Sambandamurthy and S. Banerjee, *J. Mater. Chem.*, 2011, **21**, 5580.
196 Z. T. Zhang, Y. F. Gao, Z. Chen, J. Du, C. X. Cao, L. T. Kang and H. J. Luo, *Langmuir*, 2010, **26**, 10738.
197 L. T. Kang, Y. F. Gao and H. J. Luo, *ACS Appl. Mater. Interfaces*, 2009, **1**, 2211.
198 Y. F. Sun, S. S. Jiang, W. T. Bi, R. Long, X. G. Tan, C. Z. Wu, S. Q. Wei and Y. Xie, *Nanoscale*, 2011, **3**, 4394.
199 I. N. Martyanov and K. J. Klabunde, *Environ. Sci. Technol.*, 2003, **37**, 3448.
200 I. Hyppänen, J. Hölsä, J. Kankare, M. Lastusaari, L. Pihlgren and T. Soukka, *J. Fluoresc.*, 2008, **18**, 1029.
201 R. Lopez, L. C. Feldman and R. F. Haglund, Jr, *Phys. Rev. Lett.*, 2004, **93**, 177403.
202 D. Ruzmetov, S. D. Senanayake, V. Narayanamurti and S. Ramanathan, *Phys. Rev. B: Condens. Matter Mater. Phys.*, 2008, **77**, 195442.
203 J. Liu, T. Gottschall, K. P. Skokov, J. D. Moore and O. Gutfleisch, *Nat. Mater.*, 2012, **11**, 620.
204 T. Krenke, E. Duman, M. Acet, E. F. Wassermann, X. Moya, L. Mañosa and A. Planes, *Nat. Mater.*, 2005, **4**, 450.
205 M. H. Phan and S. C. Yu, *J. Magn. Magn. Mater.*, 2007, **308**, 325.
206 V. K. Pecharsky and K. A. Gschneidner, *Appl. Phys. Lett.*, 1997, **70**, 3299.
207 M. H. Phan, S. C. Yu and N. H. Hur, *Appl. Phys. Lett.*, 2005, **86**, 072504.
208 C. N. Berglund and H. J. Guggenheim, *Phys. Rev.*, 1969, **185**, 1022.
209 O. Tegus, E. Brück, K. H. J. Buschow and F. R. de Boer, *Nature*, 2002, **415**, 150.
210 S. Gama, A. A. Coelho, A. de Campos, A. M. G. Carvalho, F. C. G. Gandra, P. J. von Ranke and N. A. de Oliveira, *Phys. Rev. Lett.*, 2004, **93**, 4.
211 P. H. Tobash and S. Bobev, *J. Am. Chem. Soc.*, 2006, **128**, 3532.
212 T. Krenke, E. Duman, M. Acet, E. F. Wassermann, X. Moya, L. Manosa and A. Planes, *Nat. Mater.*, 2005, **4**, 450.
213 M. Gatti, F. Bruneval, V. Olevano and L. Reining, *Phys. Rev. Lett.*, 2007, **99**, 266402.